Master's Thesis in Physical Oceanography

Microstructure measurements using a glider in the Faroe Bank Channel Overflow

Algot Kristoffer Peterson

June 2013

UNIVERSITY OF BERGEN
GEOPHYSICAL INSTITUTE

Acknowledgements

I would like to thank my supervisor Ilker Fer for involving me in this project, for all help and careful readings. I have definitively learned a lot through this work. Next, I want to thank my co-supervisor Jenny Ullgren, for help and support, particularly in the preparations and conduction of the cruise to the Faroe Bank Channel. Thanks to Gerd Krahmann, who willingly showed me and Jenny around, helped and answered our questions at GEOMAR in Kiel when we visited in April 2012, and for providing us with matlab-routines for the glider data. Thanks to the Institute of Marine Research in Bergen for letting us use their gliders Snotra and Gná for the fieldwork.

Thanks are also in order to the crew and other participants on the cruise to the Faroe Bank Channel in May, particularly my co-students, Elina Korssund Andrianopoulos, Tuva Fjellsbø and Mari Fjalstad Jensen for making the shift work on RV Håkon Mosby a tad more fun.

Finally, I would like to thank all students and friends in Bergen for making the life as a student so much fun, and the fellowship of students at Odd (aka the North Pole) and Høytrykket for long lunches and coffee breaks. It's been a blast.

Abstract

The application of turbulence instrumentation on underwater gliders is addressed, and two methods for glider-inferred dissipation rates of turbulent kinetic energy are evaluated against a ship-based vertical microstructure profiler. The well-established ship-based measurements are used as a reference for the analysis. A Slocum glider was deployed for one week in the Faroe Bank Channel, equipped with a MicroRider with turbulence sensors for velocity shear and temperature microstructure.

Dissipation rates of turbulent kinetic energy are calculated from velocity shear by integrating the wavenumber spectrum after fitting it to the Nasmyth universal spectrum. Survey-averaged profiles from the glider's shear-derived dissipation rates have similar shape as that measured by the vertical microstructure profiler, but overestimate dissipation rates by up to a factor of 3 in the vicinity the turbulent interface, attributed to the glider's slanted path and inability to penetrate sufficiently undisturbed through the swift plume interface.

Microstucture temperature profiles are used to calculate dissipation rates, which is done by fitting temperature gradient spectra to the universal Batchelor form using the maximum likelihood estimate. This method allows for automatic rejection criteria, which are applied to remove bad fits. Results compare reasonably well with the vertical microstructure profiler measurements, but are underestimated close to the bottom, which is a caveat of the Batchelor fit, consistent with a previous study.

Overall, measurement of dissipation rates from gliders is a powerful addition to traditional shipborne turbulence profilers, as they make it possible to survey large areas by deploying several gliders. Measurements are reasonably accurate, and require much less dedicated ship time.

Contents

Chapter 1

Introduction

In the global thermohaline circulation in the ocean, the dense, deep water masses are created at high latitudes in the Arctic and Antarctic. The dense water from the Arctic fills the Nordic Seas, which then spills over the Greenland-Iceland-Scotland ridge into the North Atlantic. The Faroe Bank Channel (FBC) is one of the two main communications across the ridge, with a sill depth of 840 m. The depth at which this water ends up depends on how much the overflow is diluted as it descends the slope. (Saunders, 2001)

Direct measurement of mixing requires high-frequency measurements of variables such as temperature or current shear. Traditionally, this is done using loosely tethered profiles, deployed repeatedly off the ship side (Seim and Fer, 2011). This provides data with little disturbance from vibrations, and repeated profiles can be made relatively fast. However, dedicated ship time is required, making it both time-consuming and expensive. Autonomous underwater vehicles, more specifically gliders, can be equipped with turbulence instrumentation, allowing continuous sampling on a low-vibration platform, and may be controlled remotely via satellite telephone. Thus, dedicated ship time is only needed for deployment and recovery, making this a potentially very useful platform for turbulence measurements (Wolk et al., 2009). Gliders move by changing their buoyancy, and translate vertical motion into horizontal motion, so they move through the water column in a zig-zag pattern, with a vertical speed favorable for turbulence measurements. Equipping gliders with fast-response shear probes and thermistors allows turbulence measurements from two independent methods on the same platform.

A field campaign to the FBC in May/June 2012 is the data foundation of this thesis, and includes data from a shipborne turbulence profiler, as well as gliders equipped with CTD (conductivity-temperature-depth) and turbulence instruments. We hypothesize that the glider is a quiet and stable platform for high-quality turbulence measurements, and that despite the slanted path of a glider, the measurements are accurate to within a factor of two, typically quoted for ocean microstructure measurements. Two methods for turbulence measurements from a glider are compared to the more established vertical microstructure profiler (VMP). Special emphasis is put on data screening and quality control of the glider turbulence data, since no

previously published studies are available on the topic.

Chapter 2 gives some general background information on gravity currents in general, and the Faroe Bank Channel in particular. Chapter 3 describes the methods, with emphasis on treatment of MicroRider data. Chapter 4 describes the field work, consisting of a test cruise in Bjørnafjorden, and the main field campaign to the Faroe Bank Channel. Results are described in Chapter 5, followed by a discussion in Chapter 6, and finally, concluding remarks in Chapter 7.

Chapter 2

Background

2.1 Gravity currents and entrainment

A dense water mass spilling over from one ocean basin to another, where it is surrounded by lighter water, will sink down along the basin's slope until it reaches buoyant equilibrium. A steady source of dense water will establish a gravity current, flowing like a river at the seabed, hereafter referred to as a dense plume. The lighter water surrounding the plume, referred to as the ambient water, is commonly assumed to be at rest. Figure 2.1 shows a sketch of a dense plume, or gravity current, and indicates positive x-direction down the slope; y- and z-directions are given following a right-handed coordinate system. Velocities are denoted u, v and w for x, y and z-directions, respectively, and a capital letter indicates a mean velocity.

As the plume descends down the slope, ambient water will mix into the plume at the interface, thus expanding the plume's volume while decreasing its density. This process of diluting the plume is known as entrainment (Turner, 1973). The driving force of this mixing process is the shear stress due to the difference in current velocity between the plume and the ambient, while the density gradient at the interface has a stabilizing effect. The ratio between stratification and shear is known as the

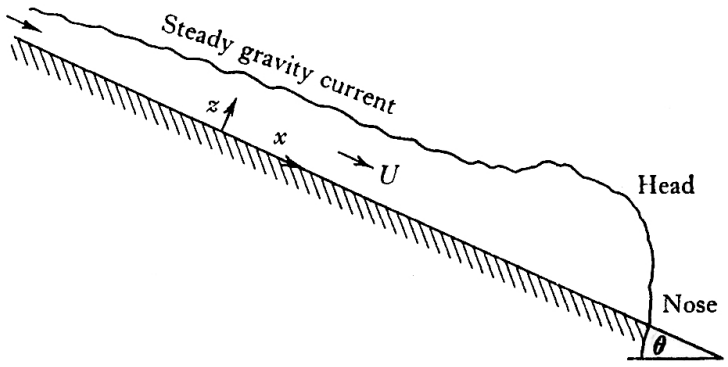

Figure 2.1: Sketch of a gravity current on a slope, with an initial head followed by a steady layer flow. From Turner (1973).

Richardson number; and in its bulk form it can be defined for our inclined plume as

$$Ri_0 = \frac{g'h\cos\theta}{U^2} = \frac{A\cos\theta}{U^3} \tag{2.1}$$

(Turner, 1973), where h is the height of the plume, $g' = g\frac{\rho_2-\rho_1}{\rho_1}$ is the reduced gravity when $\rho_2 > \rho_1$ are the densities of the plume and the ambient water, respectively, g is the gravitational constant, θ is the slope inclination and $A = g'hU$ is the buoyancy flux per unit width.

In order to quantify the amount of entrained water into the plume, an entrainment parameter is introduced. The entrainment parameter is given as a function *E(Ri$_0$)* of the bulk Richardson number, and using the continuity equation and the momentum equation, neglecting bottom friction, Turner (1973) shows that for an inclined buoyant plume,

$$E = Ri_0 \tan\theta. \tag{2.2}$$

This is a modification of the entrainment assumption, which claims that for vertically flowing buoyant plumes, the entrainment parameter can be taken as a fraction of the upward velocity, i.e. $E = \alpha W$.

Another non-dimensional number that can be used to describe the flow is the densimetric Froude number, defined as the flow speed divided by the speed of the longest interfacial wave in the two-layer system (Baines, 1995),

$$Fr = \frac{U}{(g'h)^{1/2}}, \tag{2.3}$$

which for small slopes is the inverse square root of Ri_0. The Froude number is used to determine whether a flow is critically controlled. Critical control applies for $Fr = 1$, which corresponds to where long internal waves equal the flow velocity. For $Fr < 1$ the flow is subcritical and short waves can remain stationary downstream of the sill. For $Fr > 1$ the flow is supercritical, and small disturbances cannot propagate upstream (Turner, 1973).

2.1.1 Influence of rotation

Large scale motions are affected by the Earth's rotation. The length scale at which rotational effects become important is known as the internal deformation radius, or the Rossby radius. For a two-layer fluid the Rossby radius is given as

$$L_{Ro} = \frac{(g'h)^{1/2}}{f}, \tag{2.4}$$

where $(g'h)^{1/2}$ is the speed of long internal waves, and $f = 2\Omega\sin\phi$ is the Coriolis frequency, Ω is the rotation rate of the Earth, and ϕ is the latitude (Thorpe, 2007). A plume in geostrophic balance, i.e. when the Coriolis force balances the pressure gradient force, flows along contours of constant depth. Friction violates this balance, and the plume veers across isobaths, toward deeper water. A plume restricted to a

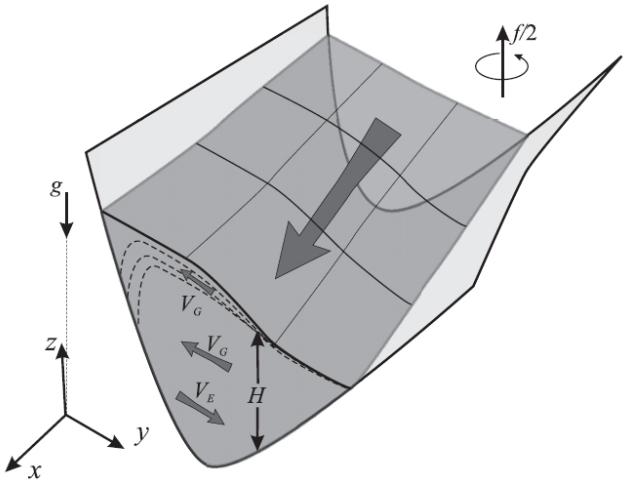

Figure 2.2: Geometry of a channelized dense plume. Down-channel velocity indicated by large arrow. V_G and V_E are the cross-channel geostrophic- and Ekman-transport, respectively. From Umlauf and Arneborg (2009).

channel will "lean" against the right-hand side, looking downstream (in the Northern Hemisphere).

The importance of viscous to rotational forces in a fluid can be determined from the dimensionless Ekman number

$$Ek = \frac{\nu_E}{2\Omega h^2}, \tag{2.5}$$

where ν_E is the eddy viscosity of water. For typical ocean values ($\nu_E = 10^{-4}\,\mathrm{m^2\,s^{-1}}$, $h = 100\,\mathrm{m}$ and $\Omega = 7.3 \times 10^{-5}\,\mathrm{s^{-1}}$) Equation 2.5 gives a small number ($Ek = 1.4 \times 10^{-4}$), indicating that rotational forces dominates over friction (Cushman-Roisin and Beckers, 2011).

Umlauf and Arneborg (2009) show the existence of a complex transverse circulation for a rotating gravity current (Figure 2.2). Friction in the bottom boundary layer (BBL) forces an Ekman-spiral with corresponding Ekman-transport (V_E) to the right. At the interface, there is an opposing geostrophically balanced transverse jet (V_G), which provides additional shear, and laterally drains the interface. This circulation pattern also explains the frequently observed pinching of interface isopycnals to the left (looking down-channel), and spreading of isopycnals at to the right (Umlauf and Arneborg, 2009; Borenäs and Lundberg, 1988; Hansen and Østerhus, 2007).

2.2 Dense Northern overflows

The dense deep waters of the world oceans are produced at high latitudes, in the Arctic and Antarctic. The water masses created through intense cooling and polynya[1] activity, convect down and spread equatorward. In the Arctic, the connection to the

[1] A polynya is a non-linear opening in otherwise ice-covered water, and is characterized by extensive heat loss, ice- and deep water production. (Brandon et al., 2009)

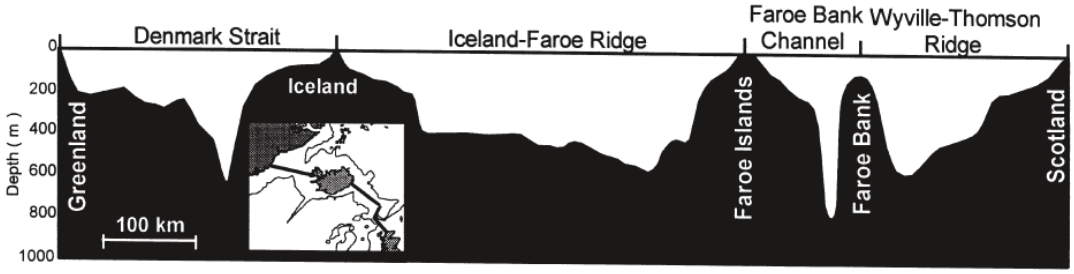

Figure 2.3: Bottom depth of the oceanic part of the Greenland-Iceland-Scotland ridge, reproduced from Hansen and Østerhus (2000)

Pacific Ocean is the shallow and narrow Bering Strait, where the mean flow is northward, and the volume transport is estimated to less than 1 Sv ($1\,\mathrm{Sv} = 10^6\,\mathrm{m^3\,s^{-1}}$) (Coachman and Aagaard, 1988). Thus the main connection southward is through the Nordic Seas into the Atlantic Ocean, separated by the Greenland-Iceland-Scotland (GIS) Ridge. As the dense water accumulates in the Nordic Seas water flows across the GIS ridge into the North Atlantic Basin. (Saunders, 2001)

The two main communications across the GIS Ridge are the Denmark Strait (DS), and the Faroe Bank Channel (FBC) (Saunders, 2001). The maximum depth of the DS is about 620 m (Hansen and Østerhus, 2000), see Figure 2.3, and its overflow carries about half of the dense water from the Nordic Seas (Girton and Sanford, 2003). However, Swift et al. (1980) found that the densest water mass, Norwegian Sea Deep Water (NSDW, see Section 2.3.1), contributes less than 10% of the overflow through Denmark Strait. The narrow FBC, lying between the Faroe Islands and the Faroe Bank, is the deepest connection across the GIS Ridge, with a sill depth of about 840 m, and is the major route for NSDW (Hansen and Østerhus, 2000).

2.3 The Faroe Bank Channel Overflow

2.3.1 Water masses

As can be seen in the temperature-salinity plot in Figure 2.4, the FBC consists of two main water masses: the cold, relatively fresher overflowing NSDW ($T \leq -0.5\,^\circ\mathrm{C}, S \approx 34.92$), and the warmer, more saline overlying Modified North Atlantic Water (MNAW) ($T \geq 7\,^\circ\mathrm{C}, S \geq 35.20$) (Borenäs and Lundberg, 1988). The intermediate water between the overflow plume and the ambient is a mixture of these two. There is also a third water mass that slightly influences the water masses in this TS-diagram, preventing a straight mixing line between NSDW and MNAW. The third water mass is most likely Arctic Intermediate Water ($T = 3\,^\circ\mathrm{C}$, $S = 34.88$) (Borenäs and Lundberg, 1988). A more thorough description of the water masses in the Faroese Channels can be found in e.g., Dooley and Meincke (1981).

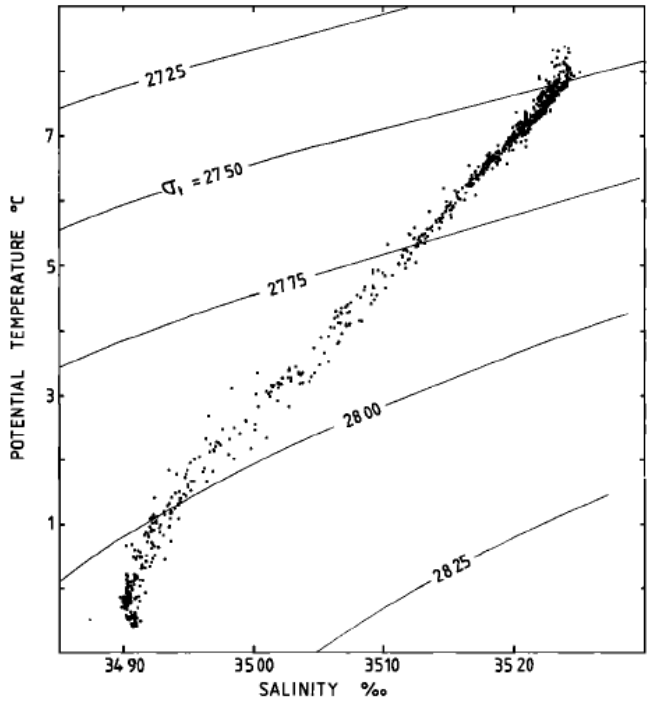

Figure 2.4: TS-diagram of water masses found in the FBC by Borenäs and Lundberg (1988), showing the two main water masses and a near-linear mixing in between them.

2.3.2 Volume flux of the FBC overflow

Saunders (1990) observed a maximum velocity close to $1\,\mathrm{m\,s^{-1}}$ in the cold overflow, and the volume flux of water colder than 3 °C was found to be in the range 1.0 Sv to 2.4 Sv. From 1995 to 2005 Hansen and Østerhus (2007) used Acoustic Doppler Current Profiler (ADCP) moorings and Conductivity-Temperature-Depth (CTD) sections to measure the FBC overflow water flux at the sill. The overflow was present every day of the 10 year long measurements, and the total overflow was estimated to be on average 2.7 ± 0.2 Sv. The volume flux of water with temperature below 3 °C was 1.7 Sv, consistent with earlier findings. They also concluded that the volume flux could be quite well estimated with only one ADCP, due to the narrow width of the channel (on the order of the Rossby radius, see Equation 2.4).

A number of studies have been published on controls on the outflow velocity. Hansen and Østerhus (2007) summarize the two main views, which are the "frictional control" and the "critical control" (also known as the "hydraulic control", see Section 2.1). The *frictional control* assumes that friction balances the baroclinic pressure gradient force. Both bottom drag and the drag from the interface between the cold overflow plume and the ambient Atlantic Water layer must be included to achieve reasonable values. The *critical control* applies when the Froude number (Equation 2.1) is unity.

Application of frictional control to the FBC overflow significantly overestimates the overflow speed ($1.6\,\mathrm{m\,s^{-1}}$ over a distance of 150 km). Critical control of FBC also overestimates overflow speed ($1.2\,\mathrm{m\,s^{-1}}$) and volume transport (2.75 Sv), but not as much as for frictional control. None of these two provide satisfactory predictions of

the FBC overflow. The width of FBC is in fact on the order of the Rossby radius, and rotational effects should be expected. Bottom topography has also been shown to be of importance, see Section 2.3.3.

Pratt (1986) use a reduced gravity model to show that friction moved the critical control point from the sill to farther downstream. For a strait of constant width, he shows that the critical point is where the slope is the negative of the drag coefficient C_d. Using several different techniques, Girton et al. (2006) find evidence that the FBC is indeed controlled, and that the critical section is located 20 km to 90 km downstream of the sill crest. Their application of cross-stream variation in local Froude number is inconclusive, as it is not sufficient that $Fr = 1$ at one station in a section; the entire section must have $Fr = 1$ (Pratt and Helfrich, 2005).

2.3.3 Entrainment and mixing of the FBC overflow

Mixing and entrainment are essential factors when studying dense overflows. Mixing reduces the maximum density of the plume, and so modifies the depth at which the overflow plume ends up. Swift (1984) gives an overview of the path of the FBC overflow, and shows how the cold overflow is diluted as it leaves the channel. Temperature-Salinity (TS) plots show a nearly linear mixing between the cold overflow and the warmer Atlantic Water it displaces (as seen in Figure 2.4). The dense overflow water, identified by Swift (1984) as $\sigma_2 = 37.04$[2], is typically found at depths near 2750 m in the northern North Atlantic.

The stress is largest at the bottom and at the interface between the dense plume and the ambient water. The bottom stress ensures that the lower part of the plume is well mixed and homogeneous, whereas the interfacial stress mixes in ambient water and expands the height and volume flux of the plume, and lowers its density.

The gradient Richardson number is the ratio of stratification to shear, given by

$$Ri = \frac{N^2}{M^2}, \tag{2.6}$$

where

$$N^2 = -\frac{g}{\rho_0}\frac{\partial \rho}{\partial z} \tag{2.7}$$

is the buoyancy frequency, ρ_0 is the reference density, and

$$M^2 = \left(\frac{\partial u}{\partial z}\right)^2 + \left(\frac{\partial v}{\partial z}\right)^2 \tag{2.8}$$

is the shear squared. Shear instabilities in a stratified flow are expected where the gradient Richardson number is less than 0.25, and this can increase the mixing significantly. From current meters and CTD measurements in the FBC overflow Borenäs and Lundberg (1988) calculated Richardson numbers at the stratified interface, sug-

[2] σ_2 is the potential density anomaly calculated for a reference pressure of 2000 dbar. For comparison, the densest water found at the FBC sill in the same campaign was $\sigma_2 = 37.42$, corresponding to $\sigma_\theta = 28.01$ at the surface reference pressure.

gesting Kelvin-Helmholtz instabilities and significant mixing. This was further supported by findings of Saunders (1990), even though he used hourly averaged current over a 200 m depth interval, with Richardson numbers in the range 0.5 to 1. Measurements with finer (10 m) vertical intervals were performed by Johnson and Sanford (1992). They used three expendable current profilers (XCP) to measure the shear. At the stratified interface they found that most of the values of Ri were around 0.25, indicating that mixing due to shear instabilities at the interface may occur, despite the strong stratification. More recent studies (Section 2.4) suggest that in addition to shear instabilities and entrainment at the stratified interface, mixing due to breaking of internal waves may also occur.

Mauritzen et al. (2005) found that the location where the overflow accelerates due to steeper topography is also where the highest mixing rates occur. This shows the importance of resolving bottom topography properly, which has also been shown by a recent high resolution observational study in the Mediterranean Sea by Nash et al. (2012). They showed that abrupt transitions from marginally stable to marginally unstable flow downstream of a 50 m drop in topography caused an increase in dissipation rates by two orders of magnitude. This was considered to be a hydraulic jump in a hydraulically controlled overflow.

2.3.4 Secondary circulation

In the bottom boundary layer (BBL) Johnson and Sanford (1992) observed very large frictional stress, a 30 m log-layer and the presence of an Ekman-spiral in the log-layer of the BBL. This was found to cause a cross-stream flow in the bottom 120 m towards south-west. The cross-stream was at its strongest about $\frac{1}{4}$ of the downstream velocity. At the interface they also found a velocity veering with height such that a cross-stream velocity was present, only in the opposite direction of the BBL. This suggested that the outflow moved down the slope with a spiral pattern where BBL water upwelled at the southwestern boundary, was transported across the interface, and experienced significant mixing.

The first direct turbulence measurements in the FBC were performed by Fer et al. (2010). These measurements confirmed the aforementioned findings of Johnson and Sanford (1992). The cross-channel Ekman transport and the compensating geostrophic transport related to the down-channel tilt of the interface had different vertical distributions, and so induced a cross-channel circulation.

2.4 Recent progress

Using the direct turbulence measurements, Fer et al. (2010) found extraordinarily high dissipation rates in the interfacial layer (IL) and in the bottom part of the boundary layer, up to $10^{-5}\,\mathrm{W\,kg^{-1}}$, see Figure 2.5. The IL was characterized by high shear and strong stratification, with $Ri < 1$, and the enhanced mixing could have been due to shear instabilities and breaking of internal waves.

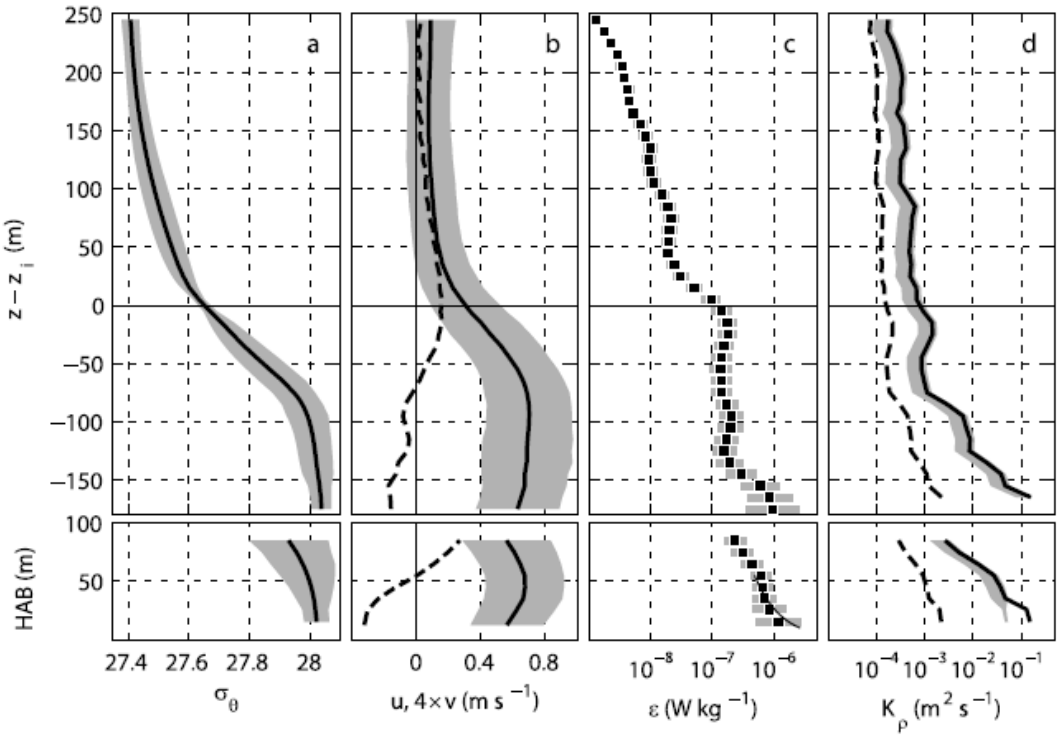

Figure 2.5: From Fer et al. (2010), showing (a) density, σ_0, (b) downchannel (u) and cross-channel (v, multiplied by 2 for clarity) components of velocity, (c) dissipation rate, ϵ and (d) eddy diffusivity, K_ρ. Profiles are averaged in 10-m vertical bins referenced to the interface depth (z_i, top), and to bottom (HAB, bottom).

Seim et al. (2010) used a state-of-the-art regional model of the FBC overflow with high resolution near the sea bed, and compared it to the measurements by Fer et al. (2010). Vertical structure of high dissipation and diffusivity near the bottom was well reproduced, where Richardson numbers were low. In the interfacial layer (IL), however, where the Richardson numbers were on the order of unity, the model highly underestimated the turbulence and mixing. This was explained by unresolved processes in the IL, where $Ri \approx 1$, primarily the transition to turbulence from internal waves, and the lack of tides in the model.

Seim and Fer (2011) showed that a secondary circulation existed also on the open slope, further downstream of the channel, similar to that discussed in Section 2.3.4, however not driven by interfacial Ekman transport, but instead the geostrophically-balanced component due to along-channel tilt of isopycnals was found to be important. Comparison with the measured transverse velocity v showed that 80% of the variability could be explained by the geostrophic component v_g. The difference between the calculated v_g and the measured v suggested a significant ageostrophic component in the opposite direction of v_g, that could have been caused by turbulent mixing in the IL.

Beaird et al. (2012) analyzed a large dataset from Seaglider deployments over three years around the GIS ridge, and inferred dissipation from finescale vertical velocity and density measurements, using a method based on a scaling of the turbulent

kinetic energy (TKE) equation (Taylor, 1935). Energy loss at viscous scales are inferred from the larger, energy-containing scales. They compared the results from this method to microstructure survey from FBC, and found the agreement between the two methods to be within a factor of two, even with dissipation ranging over several orders of magnitude. They mapped turbulent mixing in the channel remotely using gliders, and identified turbulent hot-spots in agreement with previous studies.

2.5 Glider as a platform for turbulence measurements

In addition to the indirect estimates of dissipation rates from gliders by Beaird et al. (2012), gliders may also be useful for direct measurements of turbulence parameters, such as microstructure velocity shear and temperature. The first work with Slocum electric gliders equipped with turbulence sensors was done by Wolk et al. (2009). They tested a Slocum glider, equipped with a self-contained microstructure instrument package (MicroRider) with shear probes and thermistors, in a pond with depth up to 20 m. They found the glider to be an excellent platform for turbulence measurements. The vertical speed of the glider was typically $10\,\mathrm{cm\,s^{-1}}$, nearly ideal for shear probe measurements. Vibration noise was identified from the ballast pump at the turning points, and the rudder action, but only at high wavenumbers. They were able to measure dissipation rates down to $5 \times 10^{-11}\,\mathrm{W\,kg^{-1}}$, comparable to the best tethered free-fall profilers.

The glider's slanted path may have consequences for the measurements of overturns, such as Kelvin-Helmholtz (KH) instabilities. The significance of this was recently investigated both analytically (Thorpe, 2012) and numerically (Smyth and Thorpe, 2012). Thorpe (2012) concludes that an underestimate of dissipation rates as large as a factor of 2 is unlikely for KH instabilities. Gliders with small inclination angles may also measure false overturns when gliding through internal waves, and can give misleading estimates of the scale of overturns. The modeling study found that the bias could be reduced by profiling in the cross-stream direction, and that uncertainties due to horizontal intermittency can be reduced by using ensembles of O(100).

Chapter 3

Methods

3.1 Instruments

3.1.1 Gliders

Gliders are autonomous underwater vehicles that move in a vertical saw-tooth pattern by adjusting their buoyancy and center of gravity. The two gliders Snotra and Gná used in this study are electric Slocum gliders (Jones et al., 2005) from Teledyne Webb Research[1]. The wings and tail fins of Slocum gliders translate vertical velocity into horizontal velocity, and no propeller is needed. The gliders steer by adjusting their tail rudder and center of gravity. The latter can be adjusted by moving two adjustable battery packs. The gliders are 1.5 m long, have a hull diameter of 22 cm and a mass of 54 kg (see Figure 3.2). Both gliders have an integrated SeaBird Electronics CTD (Conductivity-Temperature-Depth, SBE41). The conductivity sensor is not equipped with a pump. Additionally, Gná is fitted with a MicroRider (Rockland Scientific, Canada), designed for microstructure measurements of temperature and velocity shear. When at surface, two way communication with gliders is established through the Iridium satellite telemetry, or with FreeWave 900 MHz radio when glider is within range of the antenna. (*Slocum Glider Operators Manual*, 2011; *Slocum Glider Data Sheet*, 2010)

A glider follows a prescribed mission text file, which tells it where to go through waypoints and how deep the dives should be, along with information about which sensors should be active. Then the glider calculates the dive from its current GPS position. Each time the glider surfaces it gets a fresh GPS position fix, and calculates the offset from the previously estimated position. This information is utilized in further navigational calculations. In addition to the GPS receiver, gliders have internal compass, pressure and tilt sensors for navigation. The navigation sensor is a Micron MP50-2000. The attitude (heading, pitch and roll) sensor is a TCM3, manufactured by PNI Sensors Corporation. An altimeter in the glider is used to avoid hitting bottom, overruling the instructed depth of dive. The term 'yo' is commonly used for one single glider dive-climb. A 'double yo' is when the glider dives in a 'W'

[1] `www.webbresearch.com`

Figure 3.1: Slocum Electric glider Gná equipped with MicroRider package with microstructure sensors.

pattern, with two dives and two climbs, but only surface every second climb.

3.1.2 Ballasting

Gliders must be neutrally buoyant in the water they will be deployed in, which is achieved by ballasting. Pieces of lead, steel or similar materials with known density are attached inside the glider in the fore, center or aft sections. When the mass has been adjusted, a pump is used to create a vacuum in the glider before the ballasting is checked in a large tub with water properties similar to the site of interest. The glider is submerged, and two separate Newton meters are attached to the front and aft, ensuring that the weight of the glider in water is equal to zero. The readings from the glider's pitch and roll sensors are used to fine-tune the ballasting. Usually the weight and weight distribution must be adjusted several times before it is satisfactory. There are two adjustable battery packs in the gliders. During flight, the gliders move the central battery pack back or forth to adjust pitch, or rotate the aft battery pack to adjust roll. An air bladder is located in the aft of the gliders, which can inflate or deflate to adjust overall buoyancy, and during surfacing, it ensures that the aft fin, containing the GPS and iridium antennas, stays in air. The glider can adjust its density up to $\pm 5\,\mathrm{kg\,m^{-3}}$. The gliders Snotra and Gná used in the field work of this study were ballasted in the facilities of the Geophysical Institute in Marineholmen, Bergen.

3.1.3 MicroRider

Gná is equipped with a MicroRider-1000 from Rockland Scientific[2], which is a self-contained turbulence instrument package (Figure 3.1). It is equipped with the following sensors; two velocity shear probes (SPM-38), two fast response thermistors (FP07) and high resolution pressure, acceleration and tilt sensors (see Figure 3.2). The MicroRider is powered by the glider's battery, but stores data separately on a

[2] `www.rocklandscientific.com`

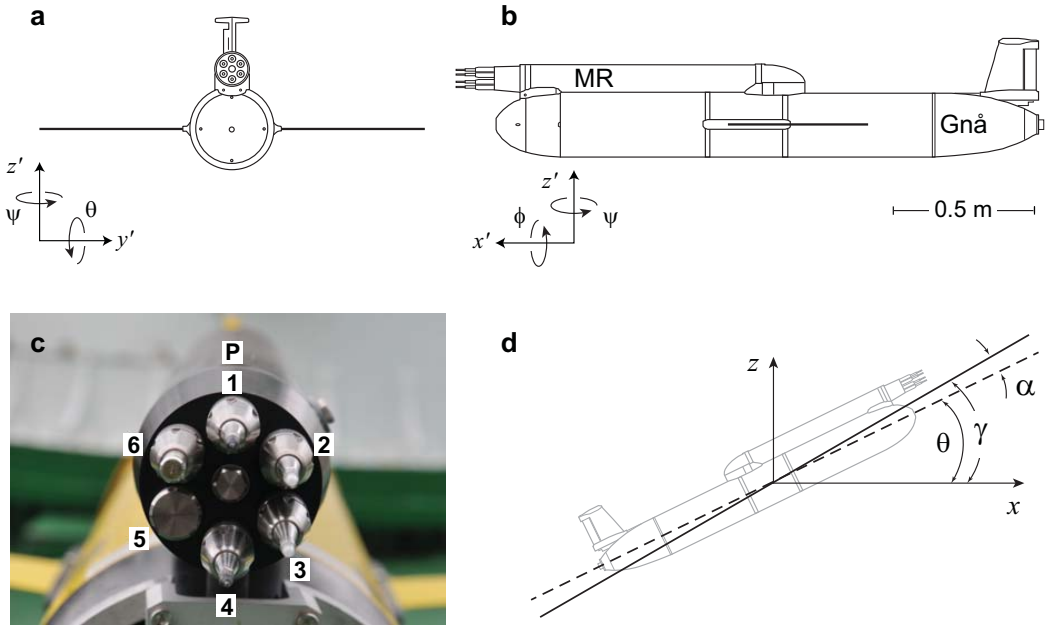

Figure 3.2: Illustrations defining coordinate system and angles (a, b and d) for Gná. (c) Shows a frontal photograph of the MicroRider. Sensors 1 and 4 are FP07 thermistors, sensors 2 and 3 are SPM-38 turbulence shear probes. Slot 5 is not in use, and 6 is a LED on/off indicator. "P" indicates the hole for the pressure sensor, located behind the other instruments.

16 GB flash card.

3.1.4 Coordinate system

The glider coordinate system is sketched in Figure 3.2, and is given relative to the glider, denoted by primes. The x'-axis goes through the glider's tail and nose, and is positive in the direction of the nose, y' points to the port side of the glider, while z' is positive upwards, perpendicular to x' and y', consistent with a right-handed coordinate system. Pitch is the angle θ between the horizontal x and the glider x'-direction, positive when the glider points upwards. Roll is the angle ϕ between the glider's y'-axis and the horizontal, positive when the port side fin is above the starboard fin. The yaw angle ψ is defined as the rotation about the glider's vertical axis z', measured relative to the glider's x'-axis, positive when the glider turns towards the port side. In terms of absolute yaw angle, it is measured relative to north. The angle of attack α is defined as the difference between the glider's pitch angle and its angle of propagation in the $x'z'$-plane, positive if the glider moves more upwards than the pitch angle.

3.1.5 Vertical Microstructure Profiler

The vertical microstructure profiler (VMP2000, VMP hereafter) from Rockland Scientific is a loosely tethered microstructure profiler for microstructure measurements in the ocean. The overall length of the VMP is 2 m, and it weighs 40 kg/3.5 kg in

air/water. The VMP is deployed using a CMK-2 hydraulic winch from Sytech Research Ltd. with Linepuller, allowing the instrument to fall freely through the water column with a fall rate of $0.6\,\mathrm{m\,s^{-1}}$. Figure 3.3 shows photographs of the VMP and the setup of the winch and Linepuller on deck. Equipped with high-accuracy CTD sensors (SBE 3F for temperature, SBE 4C for conductivity with SBE-5T pump), and high resolution sensors for micro-conductivity (SBE7-38-1 micro C), temperature (FP07-38-1 thermistor), air foil shear probes and three accelerometers. Sampling rate for the VMP is up to 512 Hz for the turbulence channels and 64 Hz for the slow channels.

3.2 Data processing

When the glider is at the surface, data files can be transferred through Iridium or FreeWave, or it can be extracted directly from memory cards when the glider is recovered. MicroRider data must be extracted directly from its flash card after recovery.

3.2.1 Glider data

The glider data are processed using the MatLab routines kindly provided by Dr. Gerd Krahmann (GEOMAR, Kiel, Germany). The processing involves the following steps.

Gliders store the data in its own format, which is converted to ASCII and then to .mat, compatible with MatLab. The .mat-files are then merged into one file. The next step is to calculate a best guess of the glider's position, based on the GPS-fixes and the glider's internal navigational calculations, and save this into the .mat-file. Then the top and bottom turns are identified from pressure, and the time series is separated into single profiles (half-yo's, e.g., one dive or one climb) and stored as elements in a structure. CTD data with timestamps before the actual dive or climb are set to NaN, and some unrealistic data are filtered out (e.g. negative conductivities). The gliders can only store one variable at each time stamp, so the time series from each sensor is interpolated to 1 s steps to ensure that each time stamp has data from all sensors.

Salinity is calculated from conductivity, temperature and pressure using the Gibbs SeaWater (GSW) Oceanographic Toolbox (McDougall and Barker, 2011). Density for surface reference pressure (σ_0) is calculated from salinity and temperature, also using GSW.

Finally, the dataset is reorganized to match the format of the MicroRider data, with several .mat-files, each containing the dives and climbs between two surfacing events (one or two of each), separated into dive- and climb-structures.

Figure 3.3: Top: The deck setup, with the winch to the right in the photograph, cable is fed to the linepuller to the left, mounted to the ship's railing. Bottom: The VMP lying on deck between deployments.

3.2.2 MicroRider data - Measuring ε

Dissipation from velocity shear

The dissipation of turbulent kinetic energy (TKE) is calculated using two different methods. One method involves direct measurements of velocity shear. Dissipation is defined as "the rate of loss of the kinetic energy of the turbulent motion per unit mass through viscosity to heat" (Thorpe, 2007), and has units $\mathrm{W\,kg^{-1}}$;

$$\varepsilon = (\nu/2)\langle s_{ij} s_{ij} \rangle, \tag{3.1}$$

which is summed over the suffices i, j from 1 to 3, and the tensor s_{ij} is given by

$$s_{ij} = \left(\frac{\partial u_i}{\partial x_j} + \frac{\partial u_j}{\partial x_i} \right) \tag{3.2}$$

where u_1, u_2 and u_3 are velocity components in an orthogonal coordinate system given by x_1, x_2, x_3. This gives a very complex expression for ε, but it simplifies significantly with the assumption of isotropic turbulence, reducing Eq. 3.1 to

$$\varepsilon = \frac{15}{2} \nu \left\langle \left(\frac{\partial u}{\partial z} \right)^2 \right\rangle. \tag{3.3}$$

With this assumption, ε may be calculated solely from high resolution vertical profiles of horizontal velocity shear by integrating the wavenumber spectrum. Because of difficulties in resolving scales smaller than the Kolmogorov cut-off length $l_K = (\varepsilon \nu^{-3})^{1/4}$, the unresolved part of the velocity shear spectrum is accounted for using the known 'Nasmyth universal spectrum' (Oakey, 1982). This is an empirical turbulence spectrum measured by Nasmyth (1970), and in practice a fitted form of this spectrum is used (Wolk et al., 2002):

$$G_2(k_n) = \frac{8.05 k_n^{1/3}}{1 + (20 k_n)^{3.7}}, \tag{3.4}$$

where $k_n = k/k_\nu$ is the non-dimensional wavenumber, k is the radian wavenumber and k_ν is the Kolmogorov wavenumber, corresponding to the Kolmogorov cut-off length l_k. Examples of this spectrum for four different dissipation rate values (ε) are shown in Figure 3.4.

Temperature gradient - Maximum likelihood spectral fitting

The second method involves the measurement of temperature microstructure. Stirring of a thermally stratified fluid induces strain, creating thermal micro-fronts, and molecular diffusion works to decrease temperature gradients. The rate of decrease of thermal variance due to diffusion of heat is

$$\chi_T = 2 k_T \left\langle \left(\frac{\partial T'}{\partial x} \right)^2 + \left(\frac{\partial T'}{\partial y} \right)^2 + \left(\frac{\partial T'}{\partial z} \right)^2 \right\rangle, \tag{3.5}$$

and is reduced to $\chi_T = 3\langle(dT'/dz)^2\rangle$ assuming isotropy (Thorpe, 2005). T' is the temperature fluctuation, and k_T is the molecular thermal diffusivity coefficient. The fast-response thermistor FP07 has a time response of 7 ms in theory, but in practice it is about 12 ms, due to diffusion and attenuation of the signal in the boundary layer around the probe. The dynamic response function used to correct the microstructure spectra is approximated by $H^2(f) = (1 + (f/f_c)^2)^{-2}$, where $f_c = (2\pi\tau W^{-0.32})^{-1}$ is the cut-off frequency, $\tau = 12$ ms is the time response of the thermistor and W is the glider's fall rate (Sirevaag and Fer, 2012; Gregg and Meagher, 1980). The temperature profile needs to resolve the Batchelor scale,

$$k_B = (\varepsilon/\nu k_T^2)^{1/4}, \tag{3.6}$$

or a sufficiently – but not completely – resolved gradient spectrum can be fitted to the universal form given by Batchelor (1959). The analytic expression for the high-wavenumber part of the temperature spectrum is (Batchelor, 1959; Ruddick et al., 2000):

$$S_B(k; k_B, \chi_T) = \left(\frac{q}{2}\right)^{1/2} \frac{\chi_T f(\alpha)}{k_B k_T}, \tag{3.7}$$

where

$$f(\alpha) = \alpha \left(e^{-\alpha^2/2} - \alpha \int_\alpha^\infty e^{-x^2/2} \mathrm{d}x \right) \tag{3.8}$$

with

$$\alpha = k k_B^{-1} \sqrt{2q}, \tag{3.9}$$

and the universal constant q has a value in the range 3.4 to 4.1 (Bogucki et al., 2012). In this study $q = 3.7$ is used, but the choice of this value is discussed in Chapter 6. Figure 3.5 shows example Batchelor spectra for variations of ε (top) and χ_T (bottom). Turbulence parameters ε and χ_T can be calculated from the temperature microstructure using the maximum likelihood estimate (MLE) fit to the temperature gradient spectrum (Ruddick et al., 2000). This method allows inclusion of an instrumental noise spectrum $S_n(k)$ in the theoretical spectrum $S_{th}(k)$,

$$S_{th}(k) = S_B(k) + S_n(k), \tag{3.10}$$

where $S_B(k)$ is the Batchelor spectrum (Equation 3.7). Another advantage of MLE over least squares, is that for non-Gaussian error distributions, least squares are often biased, while MLE estimates are unbiased. The method also reduces the number of free parameters to adjust, since χ_T is constrained by the integrated temperature gradient spectrum. Only the Batchelor cut-off frequency k_B needs to be adjusted to fit to the Batchelor spectrum, given by Equation 3.6, which is easily solved to give the dissipation rate:

$$\varepsilon = k_B^4 \nu k_T^2. \tag{3.11}$$

Rejection criteria Ruddick et al. (2000) suggest three rejection criteria to allow automated rejection of bad data segments. The first considers the signal-to-noise ratio (SNR), which is obtained by integrating the observed spectrum up to the wavenumber where noise first dominates, to the variance of the noise spectrum integrated over the same wavenumber range. If SNR is less than 1.3, the data segment should be rejected. The noise spectrum is obtained by averaging over quiescent segments. The second criterion evaluates the mean absolute deviation (MAD) of the observed spectrum S_{obs} to the theoretical S_{th}, and is given by

$$MAD \equiv \frac{1}{n} \sum_{k_i=k_1}^{k_n} \left| \frac{S_{obs}}{S_{th}} - \left\langle \frac{S_{obs}}{S_{th}} \right\rangle \right|, \tag{3.12}$$

summed up to the wavenumber k_n where signal first equals noise. A data segment should be rejected if MAD is greater than $2(2/d)^{1/2}$, where d is the degrees of freedom (DOF) of the measured spectrum. The rejection limit is twice that of a "perfect fit", as computed by Ruddick et al. (2000). A raw periodogram has $d = 2$. In order to have a segment length consistent with shear probe epsilon calculations, a 4 s FFT length (NFFT) is used. Because of the glider's slow vertical speed, a segment length S_L of 3 times the NFFT is used, giving a segment length of $3 \times 4\,\mathrm{s} \times 512\,\mathrm{Hz}$, which then leads to the degrees of freedom:

$$d_c = \frac{\text{Segment length}}{\text{NFFT}/2} = \frac{3 \times \text{NFFT}}{\text{NFFT}/2} = 6 \tag{3.13}$$

for the conservative case, with no overlaps and window smoothing. Here, however, an overlap of 50 % is used, giving 5 windows instead of 3. Effective DOF is then $d = (5/3) \times d_c = 10$.

The third criterion considers the likelihood ratio (LR), which is the maximum likelihood estimate, $\log_{10}(P_{Batch})$, compared to the maximum likelihood estimate of a power law fit, $\log_{10}(P_{Power})$. By comparing to a power law fit it is determined whether the observed data fits the curved Batchelor spectrum better than the straight line of a power law fit (see Figure 3.6). If $\log_{10}(P_{Batch}/P_{Power})$ is less than 2, the data segment is rejected.

Figure 3.6 shows an example temperature gradient spectrum (black), with a MLE fit to the Batchelor spectrum (red). The noise level spectrum is shown as a dotted line, and for comparison a power law fit (cyan) is applied to the data not dominated by noise.

3.2.3 Alignment and calibration of MicroRider data

Pressure

Pressure is measured by three different sensors on Gná; an internal navigational pressure sensor (nav-P), the CTD pressure sensor (CTD-P) and the MicroRider pressure sensor (MR-P). On the test cruise in Bjørnafjorden, the CTD-P did not work prop-

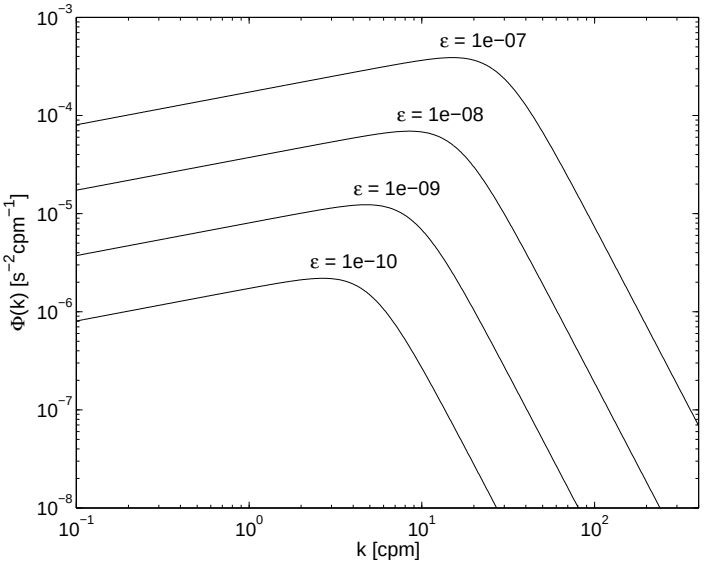

Figure 3.4: Nasmyth spectra, turbulent shear wavenumber spectrum, for varying ε [W kg^{-1}]. Spectral density [s^{-2} cpm^{-1}] is plotted against wavenumber (in cycles per meter, cpm) with logarithmic axes.

erly, so nav-P was used. In FBC, however, the CTD-P functioned, and is preferred over nav-P because of higher accuracy. First, a time lag of about 7 s between the MicroRider and the glider clocks is corrected for by comparing temperature profiles from the CTD and the MicroRider. Then the MR-P is downsampled to the glider's sampling frequency, and is calibrated against the CTD-P using a first order polynomial. Figure 3.7 shows a comparison of the pressure measurements from a full ∼900 m double yo; the original and the corrected MR-P, and the CTD-P are plotted versus time, with the nav-P subtracted to show the differences better (upper graph). Nav-P shows the lowest pressure values (except at the surface), and its discrepancy to the other measurements increases with depth to about 18 m difference to CTD-P at the deepest point. The difference between MR-P and CTD-P is shown in the lower graph in Figure 3.7, both for the original (red) and corrected (blue) MR-P. The difference between MR-P and CTD-P increases linearly with depth, until the bottom 50 m, where the increase is larger. Using a first order polynomial fit, the maximum difference is reduced from about 5 m to 2 m at the deepest point, and the linear trend is reduced significantly (and in fact, the trend is inverted).

An estimate of the error is found by calculating the root mean square (RMS) of the pressure difference between CTD-P and MR-P, both uncorrected and corrected. The largest deviations are in the steep-gradient region at the plume interface, so for comparison RMS is also calculated for all data except the steep-gradients. These areas were selected by simply excluding everything exceeding a threshold temperature-gradient of 0.1 °C m^{-1} for each dive/climb. RMS values are shown in Table 3.1. This threshold leaves out 33% of the data points. From the values it can be seen that the fit significantly reduces the RMS, and that the difference is even smaller when steep-gradient regions are excluded. The MR-P is accurate to within 0.23 dbar compared

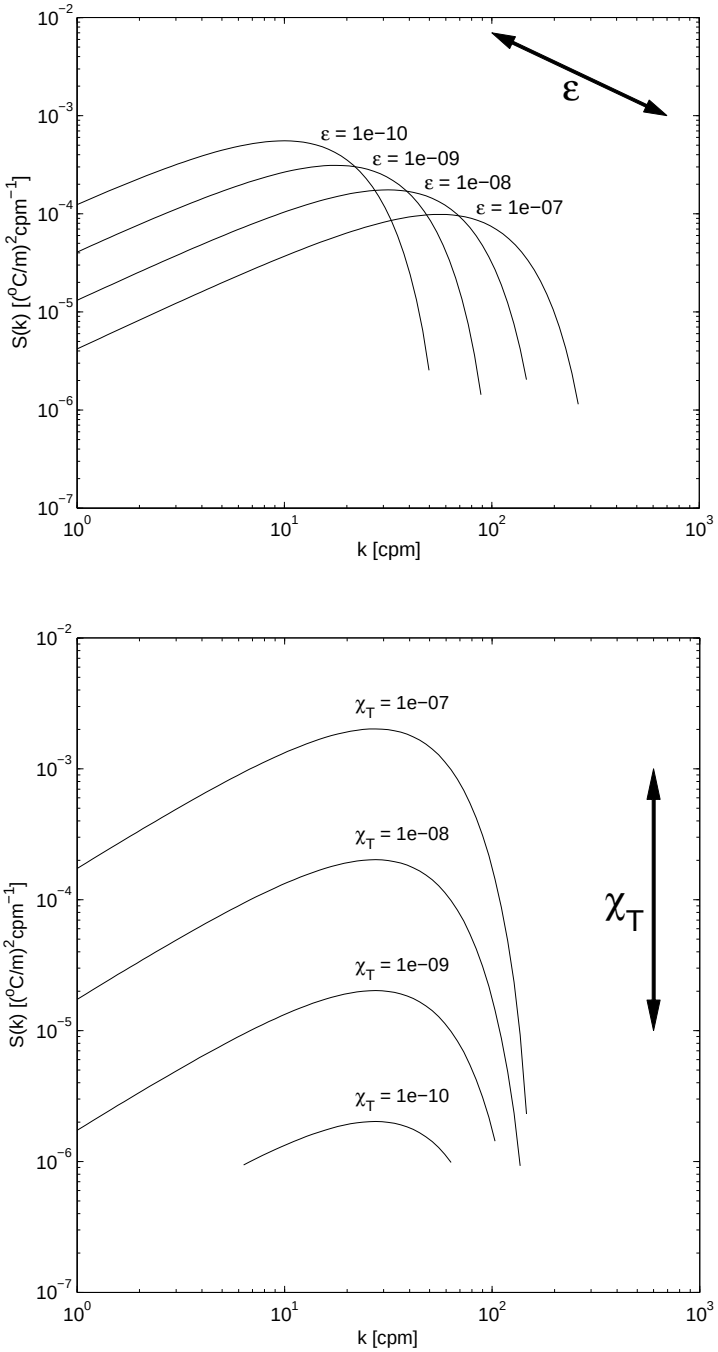

Figure 3.5: Theoretical Batchelor spectra for varying ε [$\mathrm{W\,kg^{-1}}$] and χ_T [$\mathrm{^\circ C\,s^{-1}}$]. In the top figure, χ_T is fixed at 10^{-8}, and in the bottom figure ε is fixed at 10^{-8}. Graphically, changing ε slides the graph along a -1 slope, while changing χ_T slides the graph vertically.

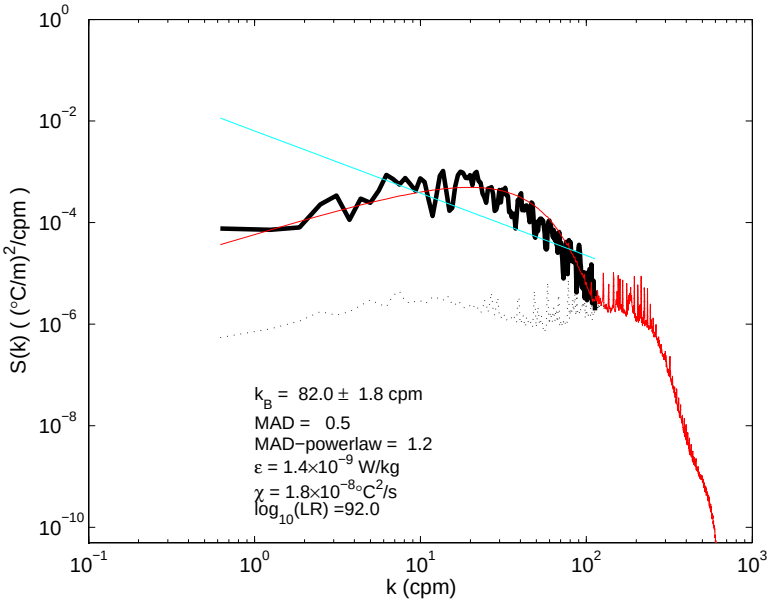

Figure 3.6: Example temperature gradient spectrum, including observed data (solid black), a Batchelor fit (red), a power law fit (straight line) and noise levels (dotted).

to CTD-P when applying the first order polynomial and ignoring the steep gradients.

Temperature

The MicroRider FP07 thermistors are designed to measure high frequency fluctuations in temperature, rather than accurate, absolute temperature. The sensors are only calibrated at surface pressure, and need to be calibrated using in situ data. Figure 3.8 shows how the MicroRider temperature (mRT, red) compares to the glider temperature (CTD-T). mRT is generally about 3 °C off, and is greatly improved by calibrating against CTD-T using a first order polynomial fit, as was done with the pressure measurements. This removes the effect of the linear pressure difference trend, as well as the mean difference. The corrected mRT is also shown in Figure 3.8 (dotted blue line). The maximum difference is reduced from about 4 °C to 0.5 °C by applying the first order polynomial (see lower graph in Figure 3.8). It is reasonable that the mRT disagrees somewhat with CTD-T in the high gradient regions because it measures at very high frequency, whereas the slow-response CTD-T will tend to smoothen the gradients.

	All data	Ignoring steep gradients
MR-P uncorrected	2.48 dbar	1.93 dbar
MR-P corrected	0.31 dbar	0.23 dbar
mRT uncorrected	3.21 °C	3.16 °C
mRT corrected	0.03 °C	0.01 °C

Table 3.1: Root-mean-square values of MicroRider pressure and temperature deviation from CTD pressure and temperature, both when using all data, and when ignoring steep-gradient regions.

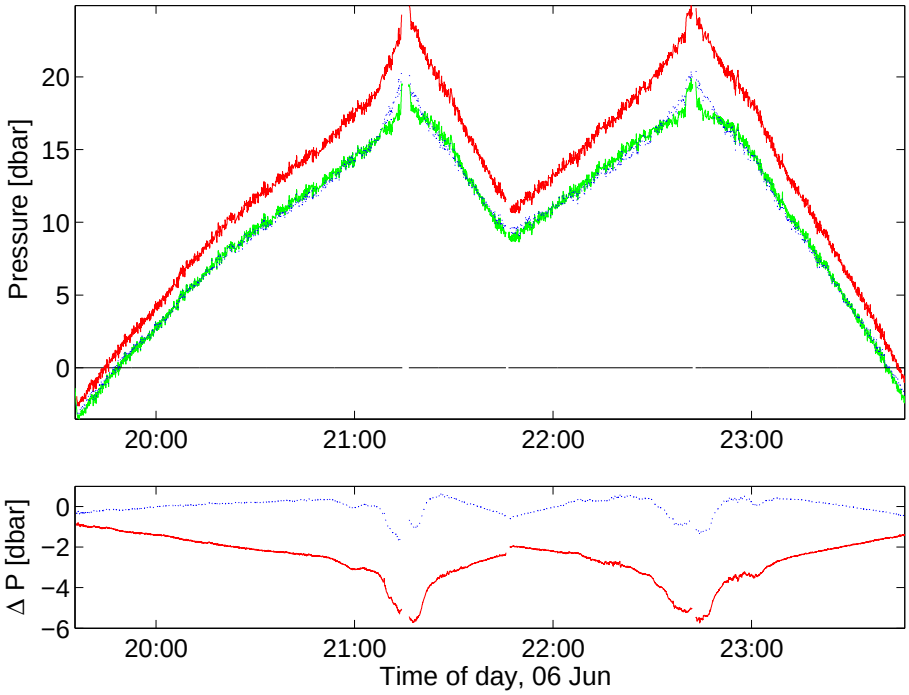

Figure 3.7: Comparison of the glider CTD (green) and the MicroRiders uncorrected (red) and linearly fitted (dashed blue) measurements of (a) pressure for a double yo. In the upper graph the glider's internal pressure sensor (nav-P) is subtracted from all measurements. The lower graphs shows the difference between CTD-P and MR-P, uncorrected (red) and linearly fitted (dashed blue).

Similar as for pressure (see above), RMS values for temperature are shown in Table 3.1, both for corrected and uncorrected mRT, for all data, and for excluding steep temperature gradients. As for pressure, the first order polynomial fit reduce the difference between MicroRider and CTD measurements, with an accuracy to within 0.01 °C compared to the CTD-T for the corrected mRT ignoring the steep gradients.

The temperature sensors are not in the exact same place, and the vertical difference in position could inflict a bias in measurements at high temperature gradients. In horizontal position, the mRT sensor is located 75 cm ahead and 20 cm above the CTD-T sensor. With a maximum pitch angle of 30°, the mRT sensor will be up to 55 cm above the CTD-T for climbs. In contrast, the CTD-T will be up to 20 cm above the mRT sensor for dives. Investigating Gná's dives, the steepest gradient over a 2 m interval was found to be on average 0.33 °C m^{-1}, giving rise to a mean maximal temperature difference between the two sensors due to vertical displacement of 0.18 °C for climbs, and 0.07 °C for dives. Figure 3.9 shows the temperature profiles used for this calculation, with the steepest temperature gradient emphasized (red).

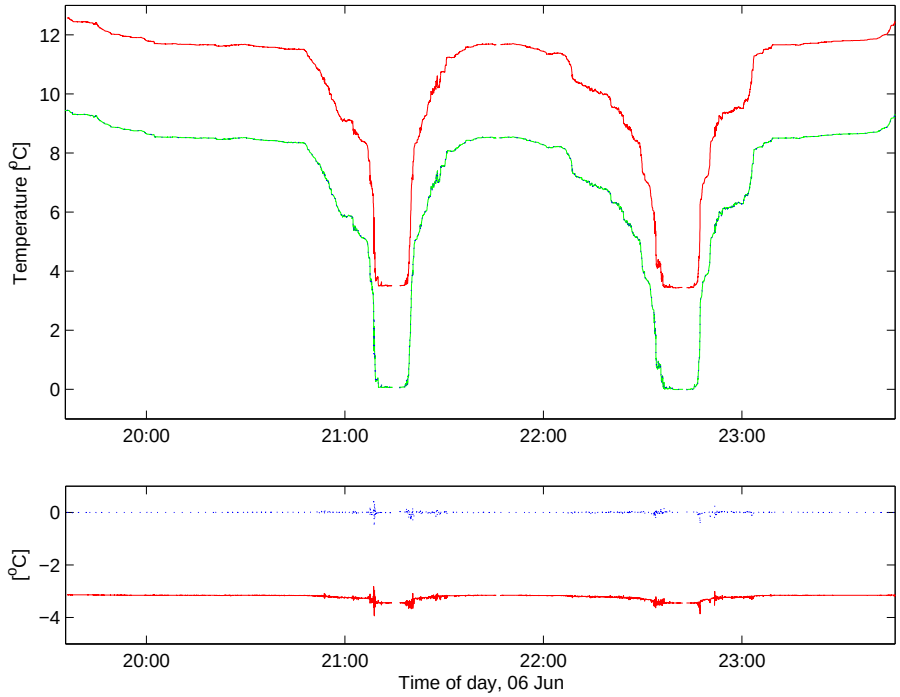

Figure 3.8: Comparison of the glider CTD (green) and the MicroRiders uncorrected (red) and corrected (dotted blue) measurements of (a) temperature for a double yo. The lower graph shows the difference between CTD-P and MR-P, uncorrected (red) and corrected (dotted blue).

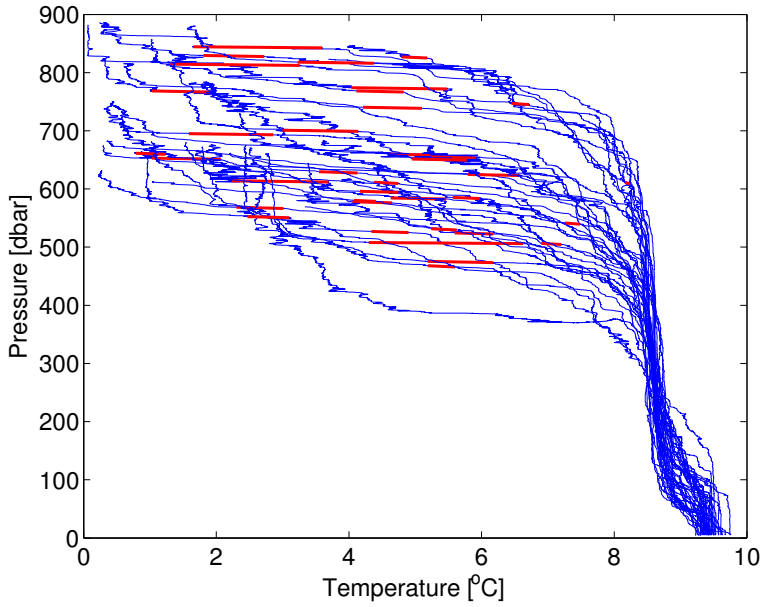

Figure 3.9: Temperature profiles used in calculating the possible difference in measured temperature due to vertical difference in instrument position. The steepest temperature gradient is emphasized in red.

3.2.4 Angle of attack

The direction the glider is moving in relative to the horizontal is called the glide angle (γ). It is defined as the glider pitch angle (θ) plus an 'angle of attack' (AOA or α),

$$\gamma = \theta + \alpha. \tag{3.14}$$

See Figure 3.2 for an illustration of the glider and the angles. The pitch angle is measured by the glider's navigation sensor, but the AOA is not measured directly. Commonly, a constant AOA is used in calculations, but this is an unfortunate assumption, as glider speed, calculated from $\partial p/\partial t$, is sensitive to this angle.

The output of the shear probe signal is proportional to the cross-stream velocity times the axial velocity when the angle of attack is sufficiently small (Osborn and Crawford, 1980). The shear is obtained by applying the Taylor frozen field assumption[3] leading to shear proportional to U^2 and shear-variance proportional to U^4, where U is the flow past the sensor, in this application the glider speed. Hence shear probe measurements are very sensitive (to the 4th power) to the glider speed and AOA.

Merckelbach et al. (2010) give an implicit expression for the AOA that can be iterated numerically,

$$\alpha = \frac{C_{D_0} + (C_{D_1,w} + C_{D_1,h})\alpha^2}{(a_w + a_h)\tan(\theta + \alpha)}, \tag{3.15}$$

where C_{D_0} is the profile drag coefficient of the glider hull, $C_{D_1,w}$ and $C_{D_1,h}$ are the induced drag coefficients of the wings and the hull, respectively, and a_h and a_w are the lift-slope coefficients for the hull and wings, respectively. Values for Slocum gliders are found in Merckelbach et al. (2010), but they do not take into account the MicroRider package mounted on Gná. Here Equation 3.15 is solved using $C_{D_0} = 0.13$, $C_{D_1,w} = 0.78$, $C_{D_1,h} = 5.5$, $a_w = 3.7$ and $a_h = 3.1$. An optimized flight model indicates drag coefficients (C_{D_0}) of about 0.13 for gliders equipped with the MicroRider when a frontal area some 30% larger than the regular glider (a_h of 0.05 instead of 0.038) is assumed (G. Krahmann, personal communication, 2012). This is a reasonable number when compared to the 0.09 to 0.11 of a regular Slocum.

3.2.5 Flow distortion

Any in-situ measurements of the velocity field will suffer from flow distortion by the instrument and the instrument platform. Wyngaard et al. (1985) studied the possible errors in velocity covariances measured ahead of axisymmetric bodies. They found that for an ellipsoid with size ratio L/D of 5:1, where L is the length, and D is the diameter, the slender-body-approximation can be applied. This allows for calculation of a flow-distortion matrix for the body, which depends on five independent distortion coefficients. Investigation of a plane at $0.5\,D$ ahead of the body revealed that errors

[3] In turbulence measurements, Taylor's hypothesis is applied, which states that the eddies are assumed not to change during the time it takes to pass the sensors. Thus, temporal measurements can be interpreted as spatial measurements.

on the order of 10 % or greater are induced for all statistics on the axis of symmetry. Errors in variances are generally decreasing with distance from the axis of symmetry, while for covariances the errors may be even larger. The approximation also showed that the flow distortion only depends weakly on small AOA.

Osborn and Lueck (1985) discussed the flow distortion effect on a research submarine. The submarine was $L = 51\,\mathrm{m}$ long, and had a diameter of $D = 5.6\,\mathrm{m}$. Their instruments were mounted $0.88\,D$ above the submarine hull, and they argued that the flow distortion should not be greater than it would be at a similar distance ahead of the submarine. Overall, they consider the effect of flow distortion on their instrument set-up negligible. Fer and Paskyabi (2013) used a Moored Autonomous Turbulence System (MATS), which is equipped with a MicroRider in its front. The platform is missile-shaped, with a length $L = 3\,\mathrm{m}$ and diameter $D = 46\,\mathrm{cm}$, which gives a shape ratio of 6.5:1. Measurements are done approximately $2\,D$ ahead of the nose, where the local diameter is 15 cm. They conclude that the effect of flow distortion is negligible compared to other error sources.

The length of the Slocum glider is $L = 1.5\,\mathrm{m}$, and its diameter is $D = 22\,\mathrm{cm}$, leading to a 6.8:1 size ratio, which fits the slender-body approximation. Because of the MicroRider, the glider is not truly axisymmetric. The turbulence sensors are located $\sim 17\,\mathrm{cm}$ ($D = 0.77$) ahead of the glider nose, and are placed off the glider axis, on top of the glider hull. A flow-distortion matrix specific for the glider-MicroRider set-up could according to Wyngaard et al. (1985) be calculated by expanding the model they used. This is not done here, and for now errors in turbulence statistics due to flow distortion are assumed to be negligible in comparison to other error sources in the measurements.

3.3 Statistical methods

Two statistical methods used in this work are described in this section. The maximum likelihood estimate is used for fitting of a theoretical spectrum to measured temperature data, and is also used to find expected mean value in measured distributions. The chi-square test is used to compare measured distributions of dissipation rates of TKE, to test whether they represent a common distribution.

3.3.1 Maximum Likelihood Estimate

The maximum likelihood estimate (MLE) is a statistical method used to find the most probable values for one or more parameters, given an observed sample and its probability density function (PDF). The *likelihood* is the joint probability density function evaluated at the observations. The maximum likelihood is where the value of the parameters in a statistic maximize the likelihood distribution. (Emery and Thomson, 2001)

Following Baker and Gibson (1986), for a sample of n independent variables in a continuous population, and given θ as a parameter of the population, the likelihood

function L is

$$L(x_1, \ldots, x_n; \theta) = f(x_1, \ldots, x_n; \theta) = \prod_{i=1}^{n} f(x_i; \theta), \tag{3.16}$$

where $f(x_1, \ldots, x_n; \theta)$ is the probability of obtaining the sample $(x_1, \ldots, x_n)$. The maximum likelihood estimator, θ_{mle}, is the value of θ that makes $L(\theta)$ maximum, which is where

$$\frac{\partial \ln L}{\partial \theta} = 0. \tag{3.17}$$

For a lognormal distribution, the maximum likelihood estimator (θ_{mle}) of the expected value is

$$\bar{X}_{mle} = \exp\left(\mu + \frac{\sigma^2}{2}\right), \tag{3.18}$$

where μ is the arithmetic sample mean

$$\mu = \frac{1}{n} \sum_{j=1}^{n} \ln X \tag{3.19}$$

and σ^2 is the arithmetic sample variance

$$\sigma^2 = \frac{1}{n} \sum_{j=1}^{n} (\ln X - \mu)^2. \tag{3.20}$$

The confidence interval is found using

$$\bar{X}_{mle} \exp\left(-\eta z_{\alpha/2}\right) < E(X) < \bar{X}_{mle} \exp\left(\eta z_{\alpha/2}\right), \tag{3.21}$$

where

$$\eta = \sqrt{\frac{\sigma^2}{n} + \frac{\sigma^4}{2(n-1)}}. \tag{3.22}$$

For a 95 % confidence interval, $1 - \alpha = 0.95$, which gives $z_{\alpha/2} = 1.96$ (Hogg and Tanis, 2010).

3.3.2 Chi-square test

To test statistically whether two measured (discrete) distributions come from a common distribution, a chi squared test may be performed. The traditional Kolmogorov–Smirnov test only applies for continous distributions, and hence cannot be performed. The chi-squared test checks the similarity of two distributions with the null hypothesis that two samples come from the same, unspecified distribution. Consider two observed data sets R and S. The data sets are separated in bins, such that there are R_i and S_i observed events from R and S in the ith bin, respectively. The chi-square statistic is then

$$\chi^2 = \sum_i \frac{(R_i - S_i)^2}{R_i + S_i}, \tag{3.23}$$

summed over all bins. A large χ^2 indicates that the null hypothesis is unlikely. The chi-squared cumulative distribution function (CDF) is calculated given the test statistic and the degrees of freedom, which depends on the number of bins. If the probability given by the CDF is less than a given significance level, say $\alpha = 5\,\%$, the null hypothesis is rejected - indicating that the two sample distributions do not come from a common distribution. If the null hypothesis is not rejected, this is not proof that the sample distributions must come from the same common distribution, it only shows that it is plausible. The probability p from the chi-squared CDF is the probability of obtaining the present distributions, or more extreme ones, given that the null hypothesis is true. (Press et al., 1992)

Chapter 4

Field Work

4.1 Test cruise in Bjørnafjorden

4.1.1 Cruise and deployments

A two day test cruise on board the research vessel (RV) Håkon Mosby was conducted between 15 and 16 March 2012 in Bjørnafjorden in Norway, approximately 40 km south of Bergen (Figure 4.1). The aim was to get familiar with the deployment and piloting, as well as to test the two Slocum electric gliders Snotra and Gná before the cruise to the Faroe Bank Channel in May 2012.

Three successful deployments were performed, first one with Snotra, and then two with Gná. The pressure sensor in the SeaBird CTD installed on Gná malfunctioned, and therefore the navigation pressure sensor data are used. The gliders are deployed and recovered using a light-boat. The wings of the gliders are attached in the light-boat to avoid damaging the gliders. Initially, a test dive to ~ 10 m depth is performed, while using a flotation attached to the glider with a long rope as a safety to check that the glider dives properly. After a successful surfacing the rope is removed and the glider is released to navigate freely.

Two CTD-stations were made using the shipborne SBE 911plus CTD, shown on the map in Figure 4.1, one on 15 March and one on 16 March.

4.1.2 Flight behavior

Figure 4.2 shows behavior data from Gná's first deployment, consisting of one single dive separated from a double dive. Pitch, and roll angles are as defined in Section 3.1.4. Typical pitch angles observed are $\pm 30°$. Roll angle should ideally be zero when the glider moves straight forward. Gná rolls slightly, about $-3°$, which is consistent with observations from the ballasting tank. The tail fin angle shows how much the glider steers, and should also be close to zero for a straight forward movement. The glider careens slightly, but the angles are typically less than $10°$. The glider adjusts its center of gravity by moving the center battery pack back and forth, which adjusts the pitch angle; i.e., pitch and battery positions are closely related. This servo controlled battery position is used in the first dive to determine the fixed

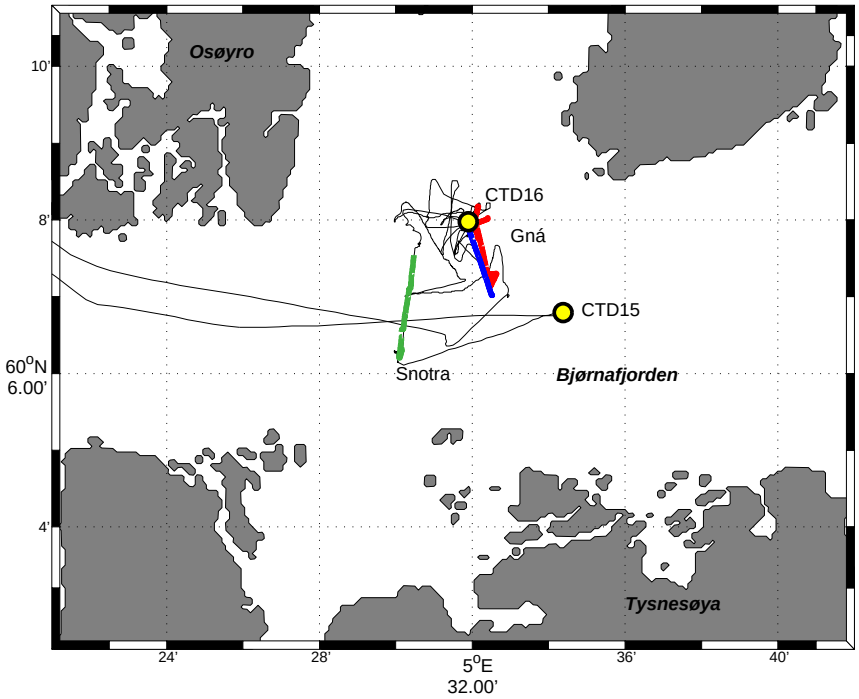

Figure 4.1: Map of Bjørnafjorden. Ship track is the black line with the two CTD stations indicated by circles. Snotra's track is shown in green, while Gná's first and second deployment in red and blue, respectively. Grid size is 3.7 km.

positions needed to maintain about ±26° pitch angles. After the first dive with Gná, these positions were set as fixed values, in order to reduce noise that can be induced in the turbulence measurements from small shifts in battery position.

4.1.3 Hydrography

Figure 4.3 shows the depth-time trace for the two deployments of Gná, color coded for temperature (top) and salinity (bottom). All dives show a slightly varying, but cold, mixed layer down to about 50 m, overlying a warmer layer with temperature maximum of about 8.5 °C around 70 m to 90 m depth. Below the maximum, temperatures are just below 8 °C. Salinity has values ranging from 30 at the surface, monotonically increasing to almost 35 below 150 m. The stratification at the site is mainly determined by salinity, and there are no salinity inversions.

Figure 4.4 shows the two CTD profiles plotted along with the nearest glider yo CTD measurements. The first ship-CTD (Figure 4.4a) was on the 15th at 12:01, while the nearest yo from the gliders were from Snotra at 14:41. This CTD station was made at a distance of approximately 4 km from the glider's position (see Figure 4.1). The second ship-CTD (Figure 4.4b) was on the 16th at 07:43, approximately 150 m from the nearest glider yo, which was from Gná at 08:59.

The temperature profiles in Figure 4.4a deviate with up to 1 °C in the upper 150 m, and a deviation in salinity and density in the surface layer. All of this is likely connected to the spatial difference between the CTD-profiles. In Figure 4.4b the profiles were much closer, and there is much more consistency in the temperature

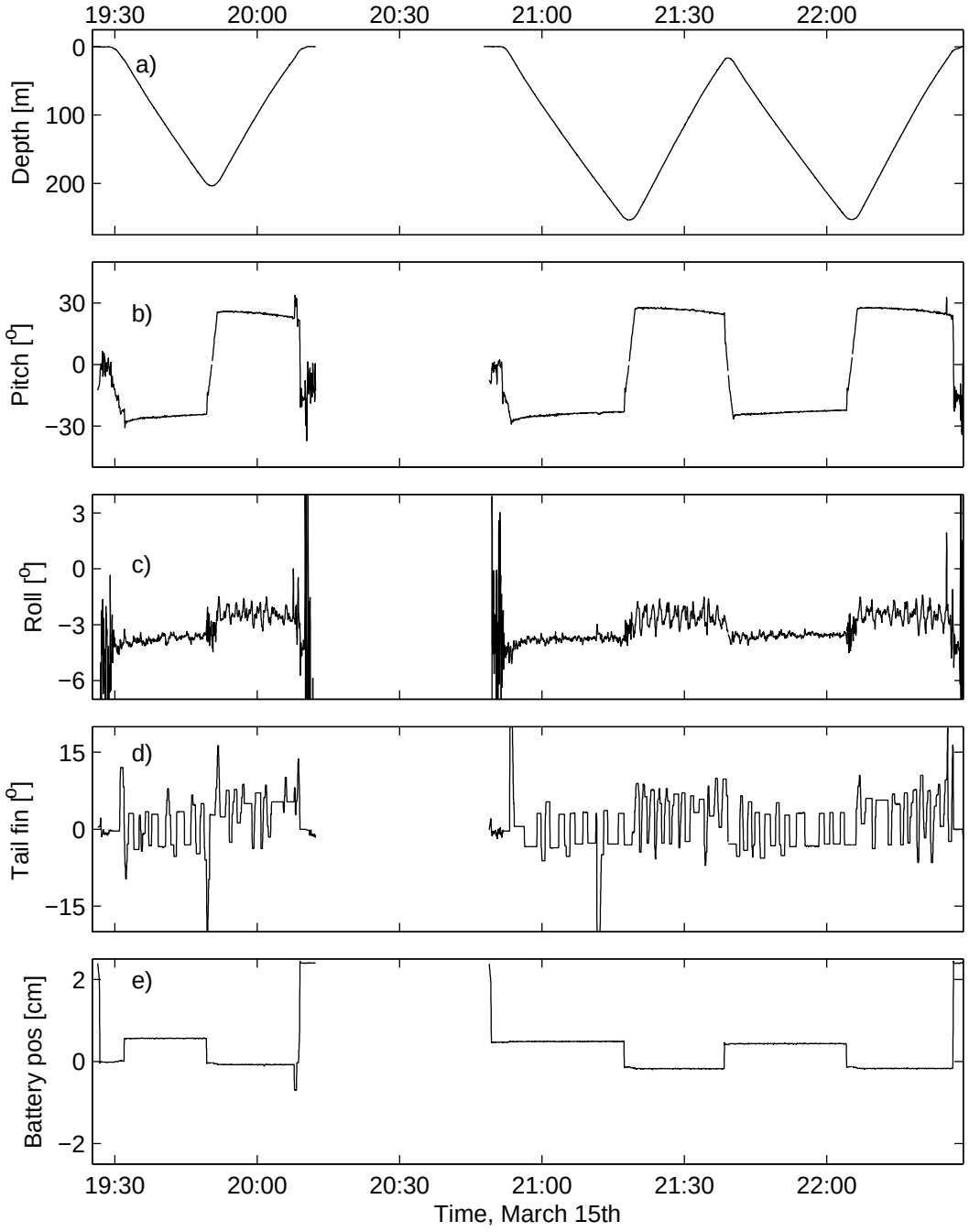

Figure 4.2: Flight behavior data from the first deployment of Gná. Time series are shown for (a) depth, (b) pitch, (c) roll, (d) tail fin direction and (e) the battery position.

data. There is, however, a systematic offset in both temperature and salinity, probably related to the trouble with Gná's pressure sensor. They are plotted here against the internal navigational pressure sensor instead of the CTD pressure sensor, which is shown in Section 3.2.3 to be systematically off with increasing depth.

Thermal lag is not accounted for in the test deployments, but this is not considered essential for the test cruise in Bjørnafjorden, as the main goal was to familiarize with the gliders, and to see that the instruments work.

4.2 Faroe Bank Channel Cruise

4.2.1 Cruise description

As a part of the project "Faroe Bank Channel Overflow: Dynamics and Mixing", a scientific cruise was conducted to the Faroe Bank Channel. The field work was conducted with the RV Håkon Mosby between 26 May and 14 June 2012, with a stop in Torshavn in 7 June. During the cruise measurements of hydrography, currents and turbulence were performed.

A total of 146 CTD/LADCP and 90 microstructure profiles were made during the cruise. The CTD was a SBE 911plus from SeaBird Inc[1]. Two LADCPs (Lowered Acoustic Doppler Current Profiler, Workhorse Sentinel 300 kHz ADCP from Teledyne RDI[2]) were mounted on the CTD rosette; one looking up, one looking down. The LADCPs were operational on 143 of the 146 stations. The two Slocum electric gliders Snotra and Gná were deployed for the duration of the cruise. They were both equipped with CTDs, and additionally Gná was equipped with a MicroRider from Rockland Scientific. The instrument is described in detail in Sections 3.1.1 and 3.1.3.

Figure 4.5 shows a map of the study area and tracklines of the two gliders Snotra (red) and Gná (yellow). The dates 4, 6 and 8 June are marked with circles. Figure 4.6 shows the positions of CTD stations, with colors indicating the different sections. The stations T1, M1 and B4 (white circles) were made as time series by repeating CTD-deployments hourly for up to 12 h.

4.2.2 Glider behavior

The gliders were instructed to sample cross-sections of the plume, but the strong plume current at depth made precise navigation very difficult.

Figures 4.7 and 4.8 show glider flight behavior from Gná and Snotra on 6 June, covering time series of depth, pitch, roll, tail-fin angle and battery position. The pitch angle is stable at $\pm 30°$ for climbs/dives. Roll is generally more variable, with typical amplitudes of 2°. On 4 June, Gná was out of track, and reported roll variations of as large as 12°. Upon inspection, her port wing was twisted and the wing holder was loose. Replacing the wing reduced the roll variation to 2° again, but the mean roll was shifted to about 11°.

[1] www.seabird.com
[2] www.rdinstruments.com

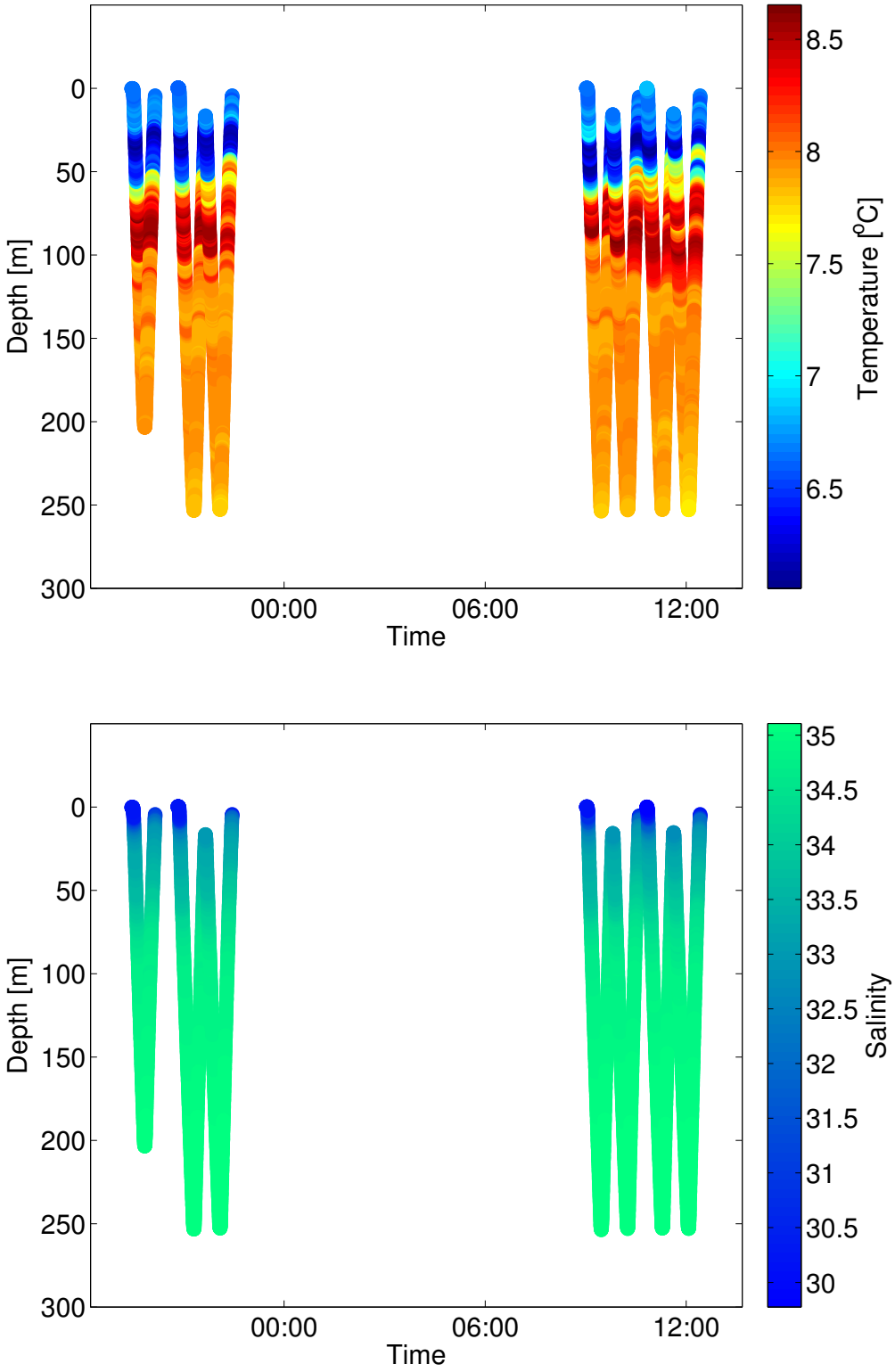

Figure 4.3: The vertical saw-tooth pattern from Gná on the test cruise. Glider depth is plotted versus time, color coded for (top) temperature and (bottom) salinity with the scale given on the right.

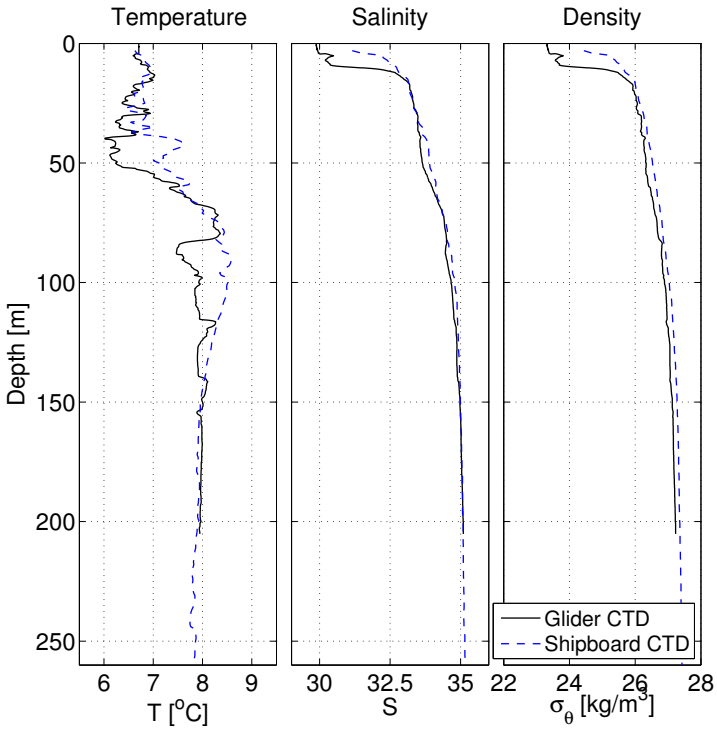

(a) 15 March

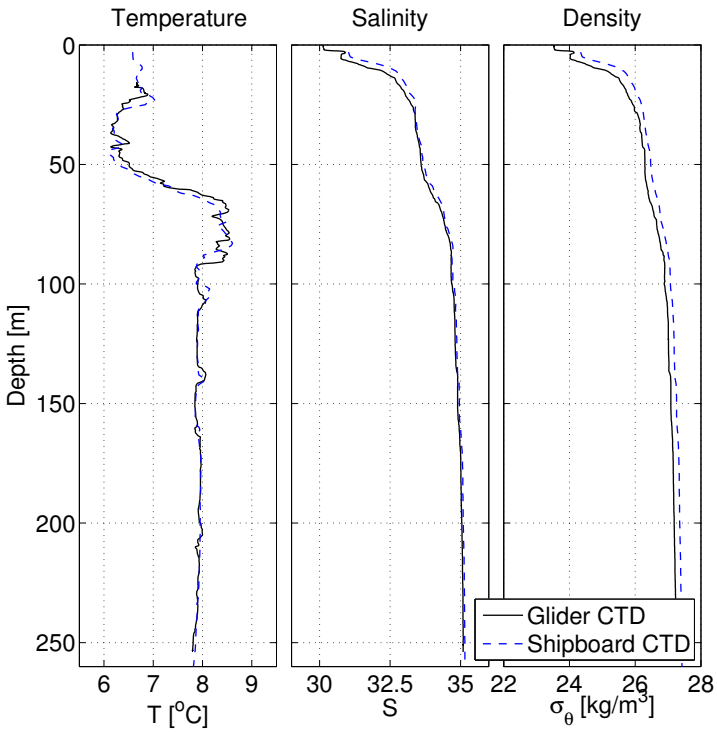

(b) 16 March

Figure 4.4: CTD profile comparison from Gná (solid black line) and shipboard CTD (broken blue line) for the (a) first and (b) second deployment. See map in Figure 4.1 for the station positions.

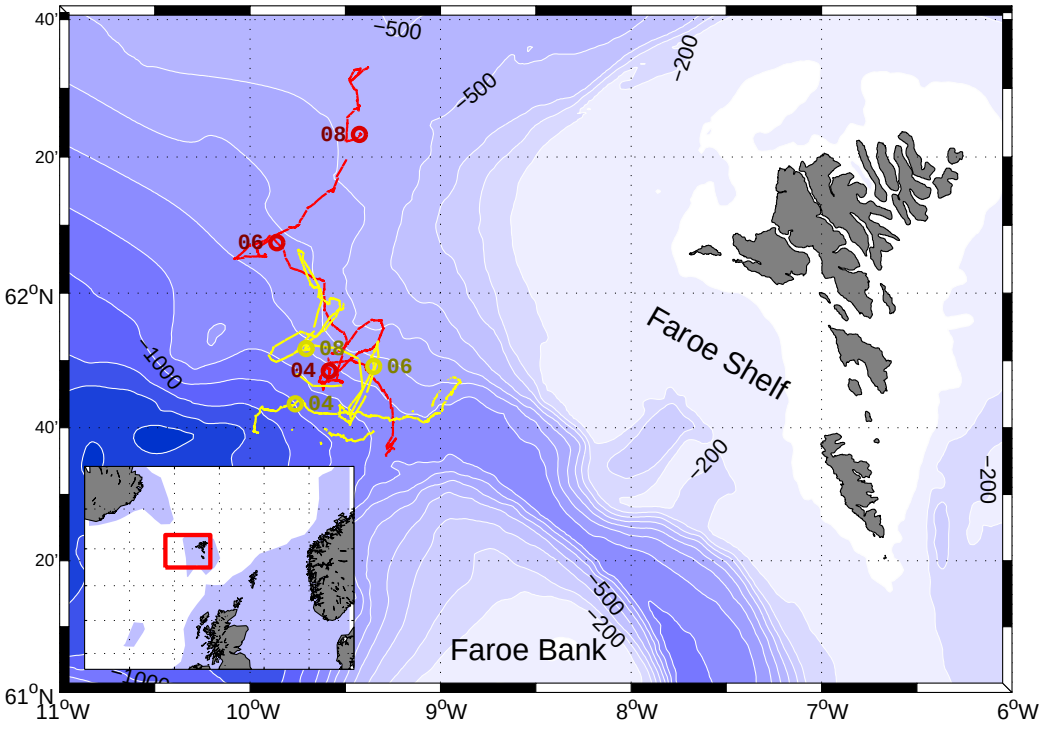

Figure 4.5: Map with tracklines of Snotra (red) and Gná (yellow), with their positions on 4, 6 and 8 June marked with circles. Depth contours every 100 m. In the insert map, depths less than 500 m are shaded blue.

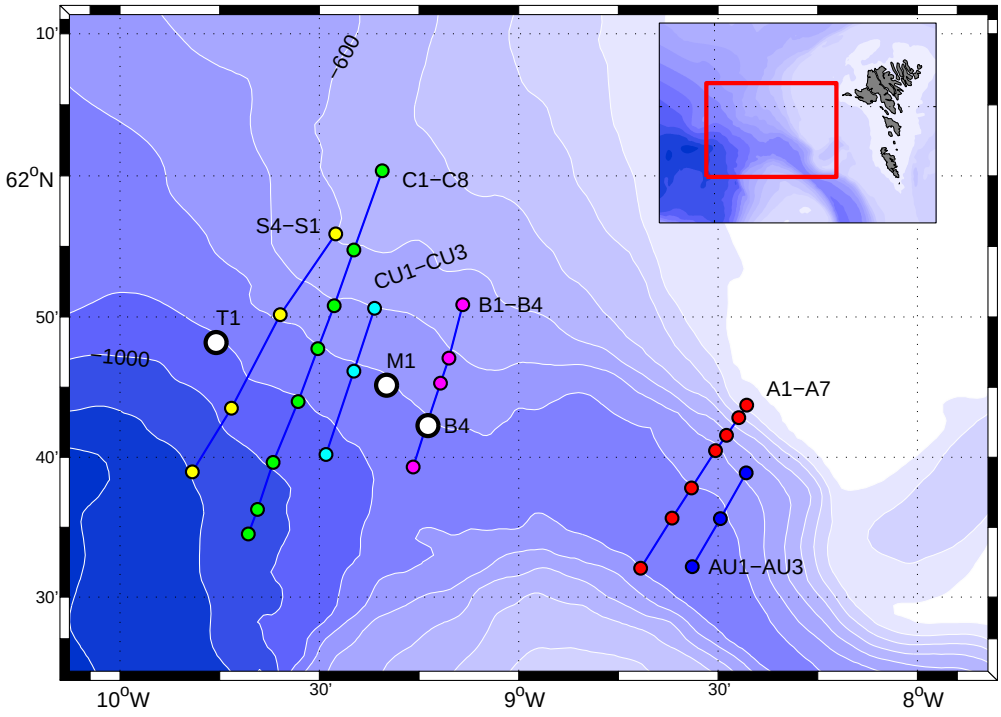

Figure 4.6: Map with the CTD stations indicated. White markers T1, M1 and B4 are yo-yo stations, all sections have separate colors, and the sections A1-7, AU1-3, C1-8, CU1-3 were repeated several times during the cruise.

The gliders adjust the pitch for dives and climbs by changing the battery position. On Snotra, the battery position was controlled by the servo, while Gná was manually set at fixed positions for climbs and dives (as described in Section 4.1.2). The frequent change in battery position caused by the servo creates vibrations which affect the quality of turbulence measurements. Comparison of the lower panel in Figures 4.7 and 4.8 shows the effect of setting fixed battery positions as opposed to using servo.

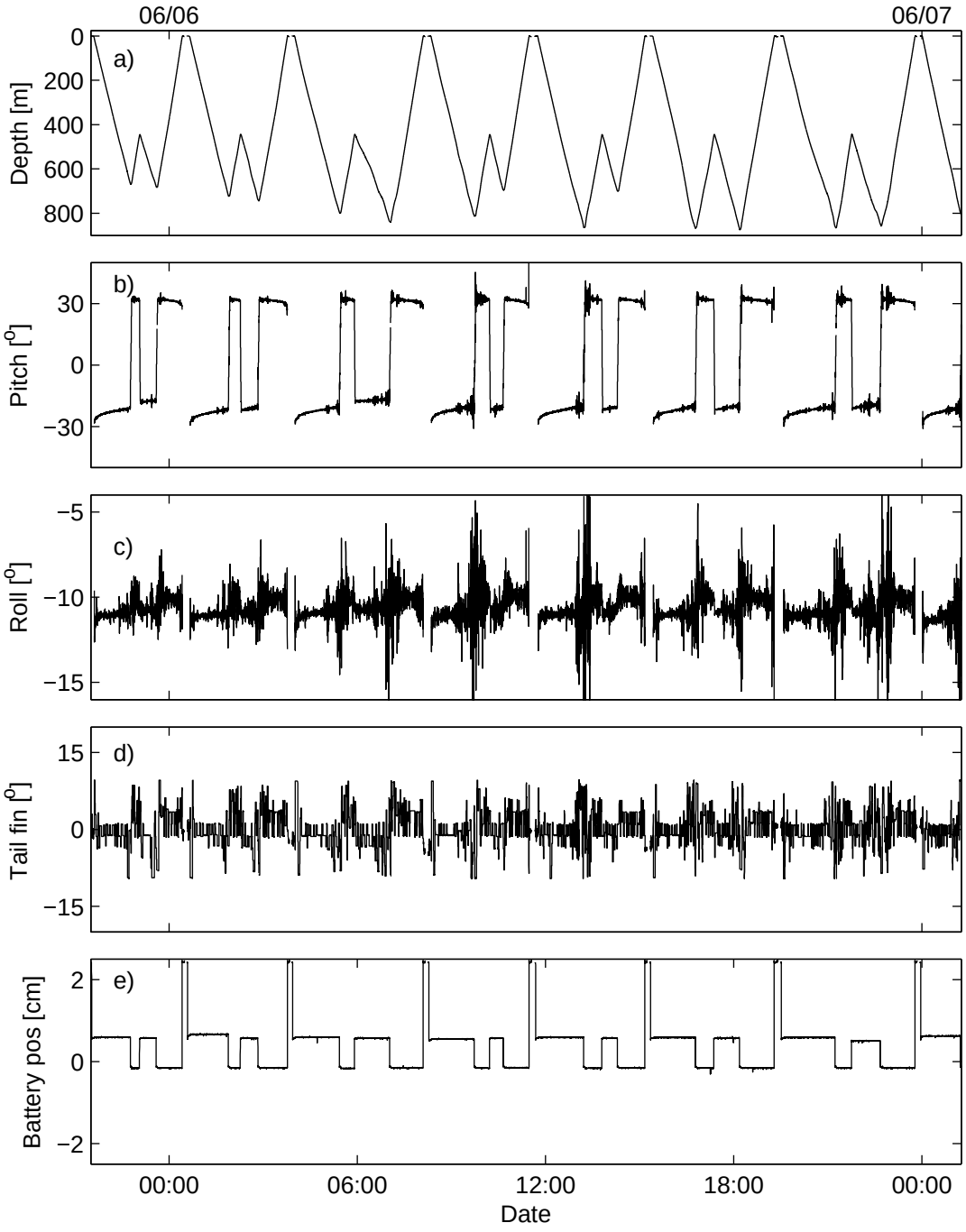

Figure 4.7: Flight behavior data from Gná on 6 June: (a) depth, (b) pitch, (c) roll, (d) tail fin direction and (e) the battery position.

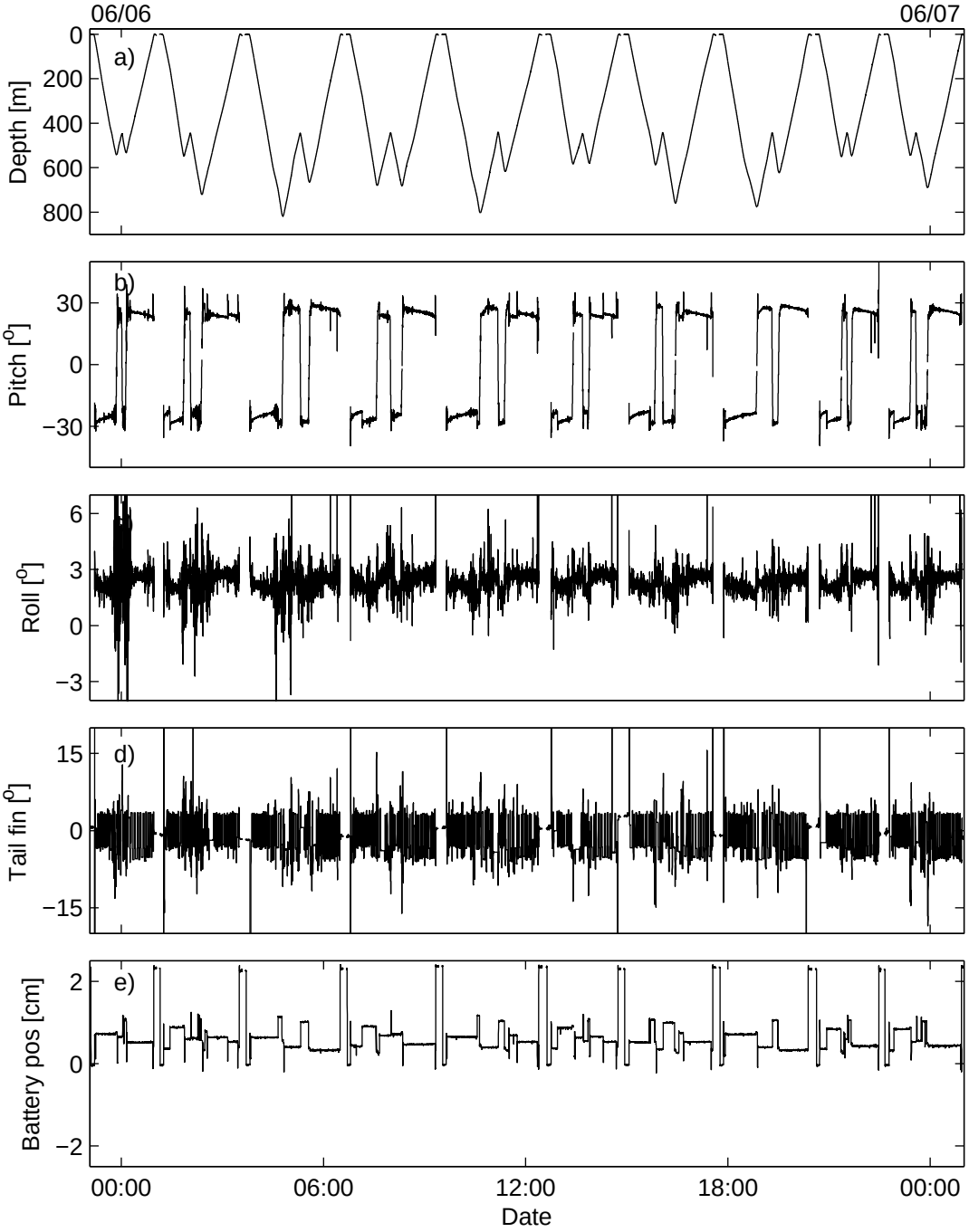

Figure 4.8: Same as Figure 4.7, but for Snotra.

Chapter 5

Results

5.1 Overview of oceanographic conditions

5.1.1 Hydrography and currents

An overview of the oceanographic conditions is given by looking at two sections in the study area, sections A and C (Figures 5.1 and 5.2), where section C is approximately 50 km downstream of A (see map in Figure 4.5). Along the bottom, a plume of cold water is observed, with temperatures between 0 °C and 3 °C and current velocities up to $1\,\mathrm{m\,s^{-1}}$ are found in both sections. The interfacial layer is visible as a strong thermocline between approximately 150 m to 300 m above the bottom. Above the interface, temperatures are much higher, in the range 7 °C to 10 °C. The overflow plume leans to the right hand slope. The current is bottom-intensified in the downstream section, but in the upstream section the strongest current is found between 50 m to 100 m above the bottom. Outside the plume, the currents are weaker, and in some places in the opposite direction. In the downstream section the plume is more widespread, and thinner, compared to the upstream section.

Figure 5.3 shows survey-averaged hydrography data measured by Gná, separated into dives (red) and climbs (blue). Profiles of temperature, salinity and potential density anomaly are depth-averaged in 1 m bins, with respect to height above bottom (HAB) for the bottom 400 m. In the top graph temperature is plotted against salinity (TS-plot), and the bottom graphs show profiles of temperature, salinity and density with respect to HAB. Because the CTD is not pumped, a systematic offset in salinity between dives and climbs can be seen in Figure 5.3. This can be corrected for (see Garau et al., 2011), but this is not done here, as there is a very tight temperature-salinity relation, allowing density to be inferred from temperature alone. There is an almost straight mixing line between the warm, saline water at the surface, and the cold, slightly fresher water at the bottom. This indicates that only two main water masses are present in the FBC.

Figure 5.4 shows a map with all glider dives deeper than 600 m, color coded for the lowest recorded temperature in each glider yo. The lowest temperatures are generally found at the bottom. Bottom temperatures between 0 °C to 1 °C are most common,

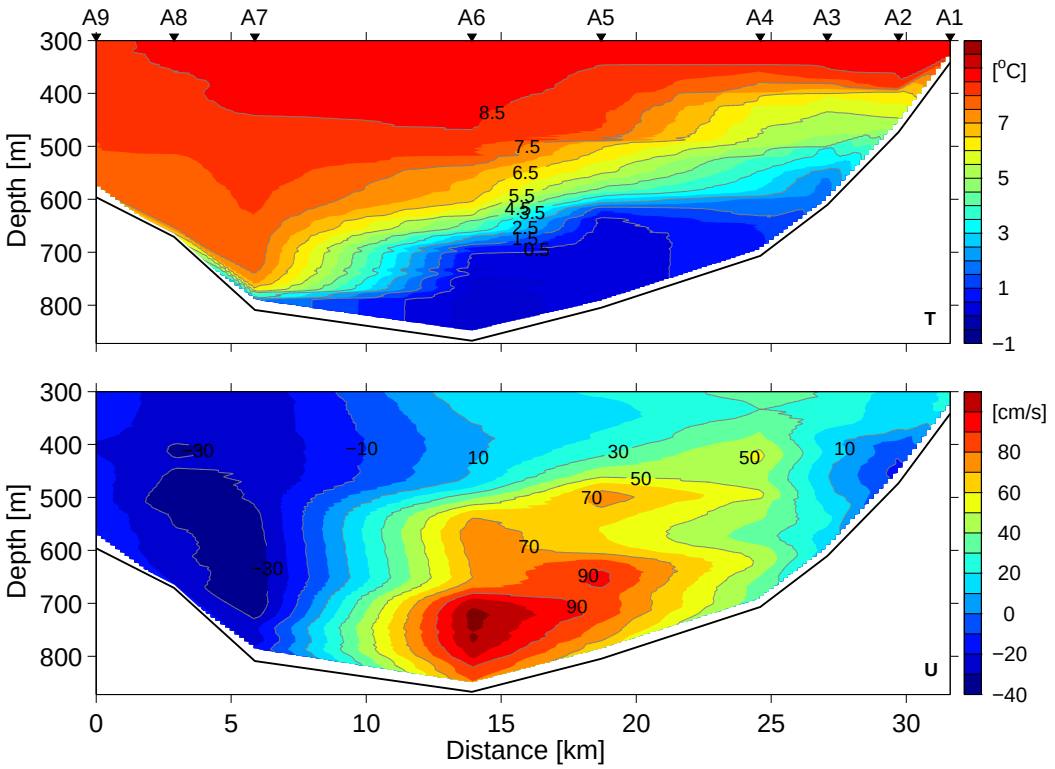

Figure 5.1: (Top) Contour plots of temperature (T) from shipborne CTD and (bottom) downstream current velocity (U) from LADCP for section A. Plume flow direction is into the paper, with north-east to the right. The top 300 m are not shown. Arrowheads at the top mark the stations indicated by numbered letters. See Figure 4.6 for section location.

but some places temperatures up to 8 °C are the coldest, even for dives deeper than 600 m.

5.1.2 Plume structure and turbulence

Figure 5.5 shows a profile from the LADCP current measurements at station CU1 (see map in Figure 4.6), the red and blue lines show the along-stream (U) and cross-stream (V) current components, rotated into the mean direction of the 10 % strongest current measurements in the profile. The panel on the right hand side shows a profile of density for the same station. The horizontal red line indicates the top of the boundary layer (BL), estimated as the height where the density difference from the value at the bottom first exceeds 0.01 kg m^{-3}. A layer called the stratified interfacial layer (IL) is defined as the layer between the top of the boundary layer (BL top) and the height above this where $\partial\sigma_\theta/\partial z$ first drops below 5×10^{-4} kg m^{-4} (Fer et al., 2010). The density profile is sorted to ignore inversions in the above definitions, but the inversions are marked with red triangles in the density profile, scaled by the density anomaly (i.e. the larger the triangle size, the larger the density difference). Most of the inversions are located in the IL, where shear instability and Kelvin-Helmholtz billows are expected. Mauritzen et al. (2005) suggest the

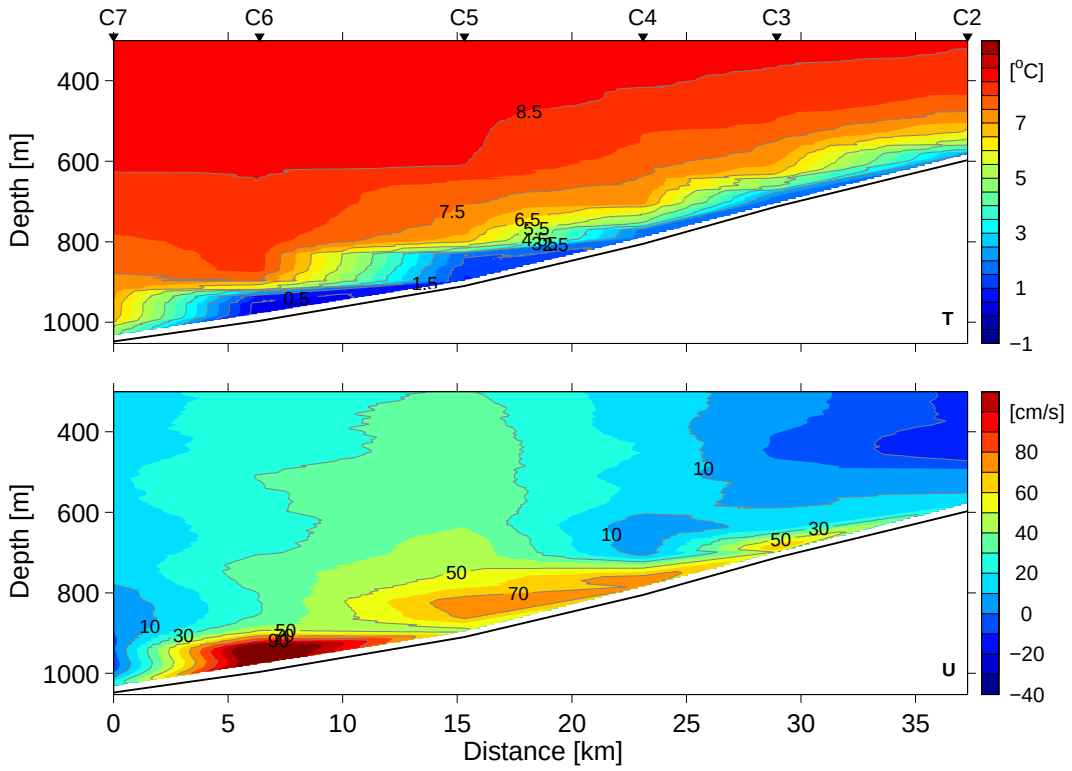

Figure 5.2: Same as Figure 5.1, but for section C, about 50 km downstream of A. Note different axes.

$\sigma_T = 27.65\,\mathrm{kg\,m^{-3}}$ isopycnal ($T <\sim 3\,^\circ\mathrm{C}$) as a useful divider between the plume and the overlying Atlantic Water, shown here as a black, horizontal line, about 145 m height above bottom.

Figures 5.6 and 5.7 show the rate of dissipation of turbulent kinetic energy, $\log_{10}(\varepsilon)$, for sections A and C, respectively. It is shown interpolated both with respect to depth and to height above bottom (HAB). Interpolation with respect to HAB removes the unrealistic horizontal bands of large dissipation rates close to the bottom seen in the depth section. The downstream section C shows the highest dissipation rates, up to $\varepsilon \sim 10^{-5}\,\mathrm{W\,kg^{-1}}$ in the bottom boundary layer. High dissipation rates are also found in the interfacial layer, approximately 200 m above the bottom. High dissipation rates coincide with high current shear. Extrapolating dissipation rates to the bottom for sections A and C, approximately 4.8 % and 6.9 % of the data within 200 m above bottom have $\varepsilon > 10^{-6}\,\mathrm{W\,kg^{-1}}$, respectively. The geometric mean values for the sections A and C are about $1.0 \times 10^{-8}\,\mathrm{W\,m^{-2}}$ and $6.3 \times 10^{-9}\,\mathrm{W\,m^{-2}}$, respectively.

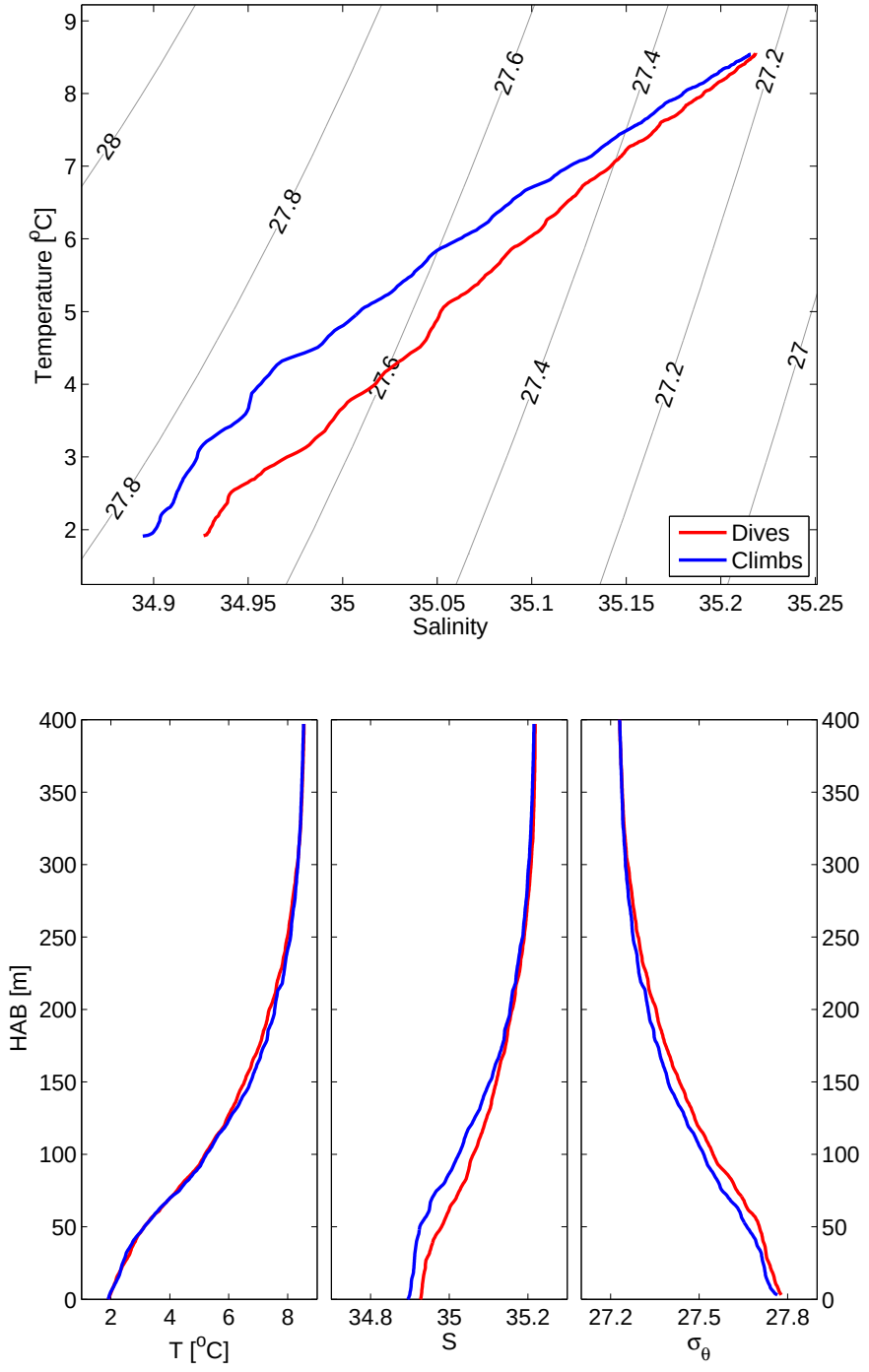

Figure 5.3: Survey-averaged hydrography data measured by Gná. (Top) Temperature-Salinity diagram and (bottom) vertical profiles of temperature, salinity and potential density anomaly, σ_θ, averaged with respect to height above bottom (HAB)

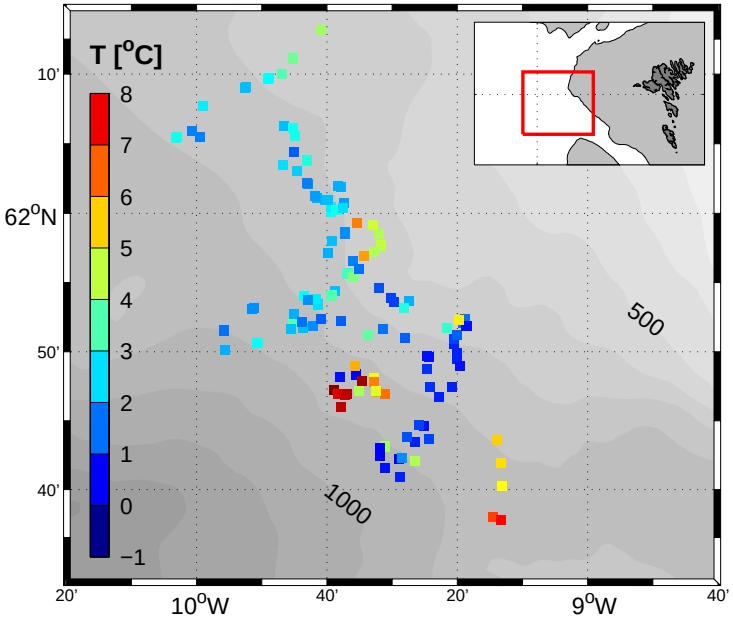

Figure 5.4: Map showing the lowest recorded temperature (in °C) in each yo as a color coded dot with a scale to the right. Data from both Snotra and Gná is included, but yo's with maximum depth less than 600 m are excluded. Depths < 500 m are shaded in the insert map.

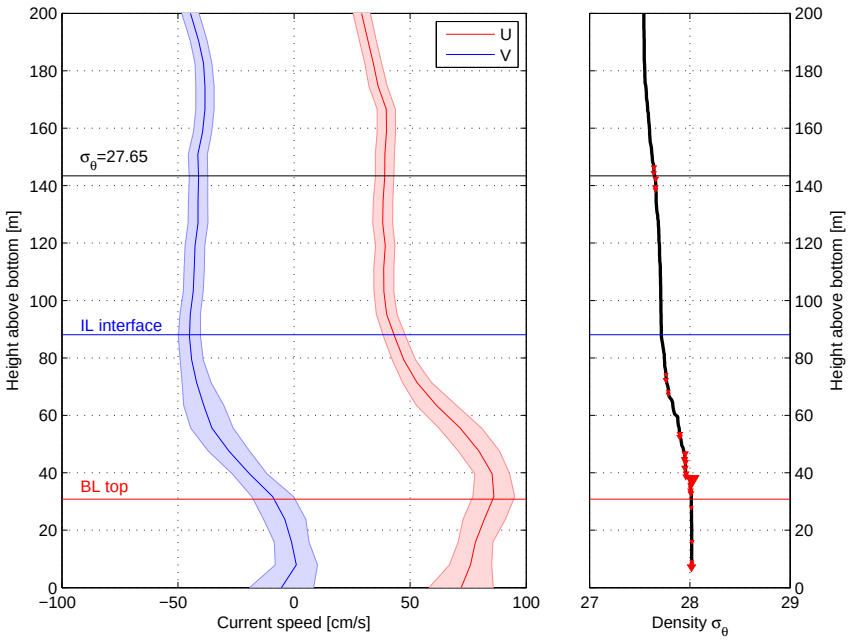

Figure 5.5: LADCP current profile from station CU1 (see Figure 4.6), with the shaded error bars from LADCP processing. The vectors are rotated into the mean direction of the 10 % strongest current vectors in the profile. To the right, the density profile is shown in black, with inversions marked as red triangles, scaled by the density difference.

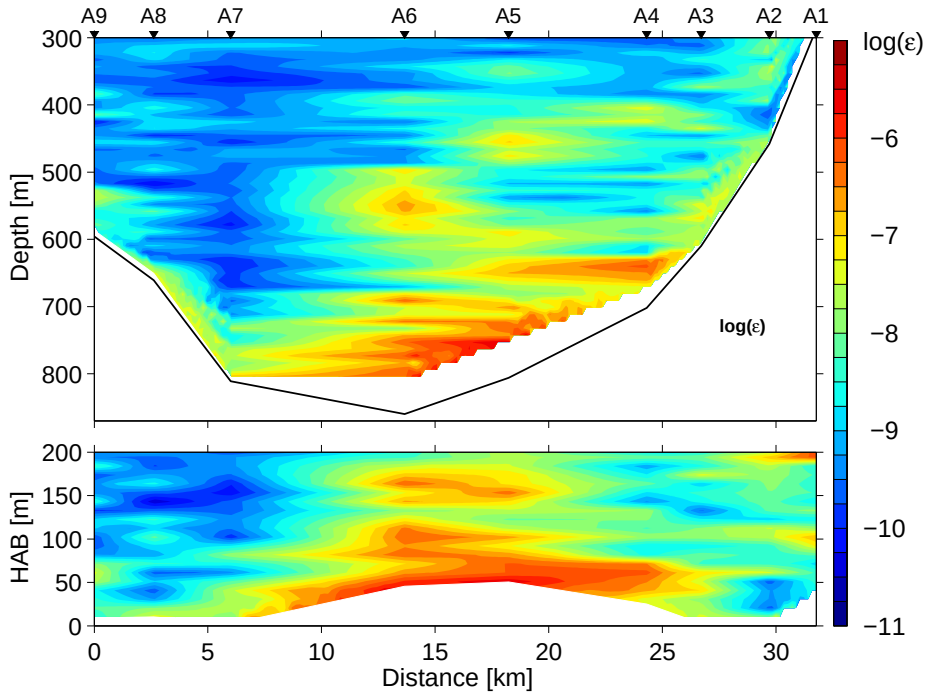

Figure 5.6: Cross section A of the study area, showing rate of dissipation of turbulent kinetic energy, $\log(\varepsilon)$ in $\mathrm{W\,m^{-2}}$, as measured by the VMP, plotted with respect to depth (top) and height above bottom (HAB, bottom). Arrowheads at the top mark the stations indicated by numbered letters. Plume flow direction is into the paper, with the North-East to the right in the figure. The x-axis is ticked every 5 km, and the black line indicates the corrected depth from the ship's echo sounder. The top 300 m is not shown in the upper figure.

5.2 Turbulence measurements with gliders

5.2.1 Data screening: Shear probes

Some of the calculated dissipation rates from shear probes may be unreliable, for instance in regions where the glider encounters navigational problems, such as when entering the plume. There is also reason to separate dives and climbs, e.g. the gliders can experience difficulty in penetrating the plume, but not leaving it. In order to identify thresholds for excluding unreliable dissipation rate data derived from shear-probe turbulence measurements, navigational variables are plotted against ε in Figure 5.8. For variables where high/low values are associated with high dissipation rates, unreliable data can be removed by setting rejection criteria for that variable. In the scatterplot of angle of attack (AOA) against ε (Figure 5.8, upper left), there is a clear difference between dives and climbs: AOA is higher for dives, and is scattered in two clusters. For AOA greater than 4.5° the dissipation rates are corrupted, biased high. For climbs, AOA is generally lower, and is less scattered. Several outliers are associated with AOA$>$ 1.8°.

The applicability of Taylor's hypothesis can be violated when $|W|$ is small. Turbulent eddies may then not be advected past the sensors, and the instrument may be

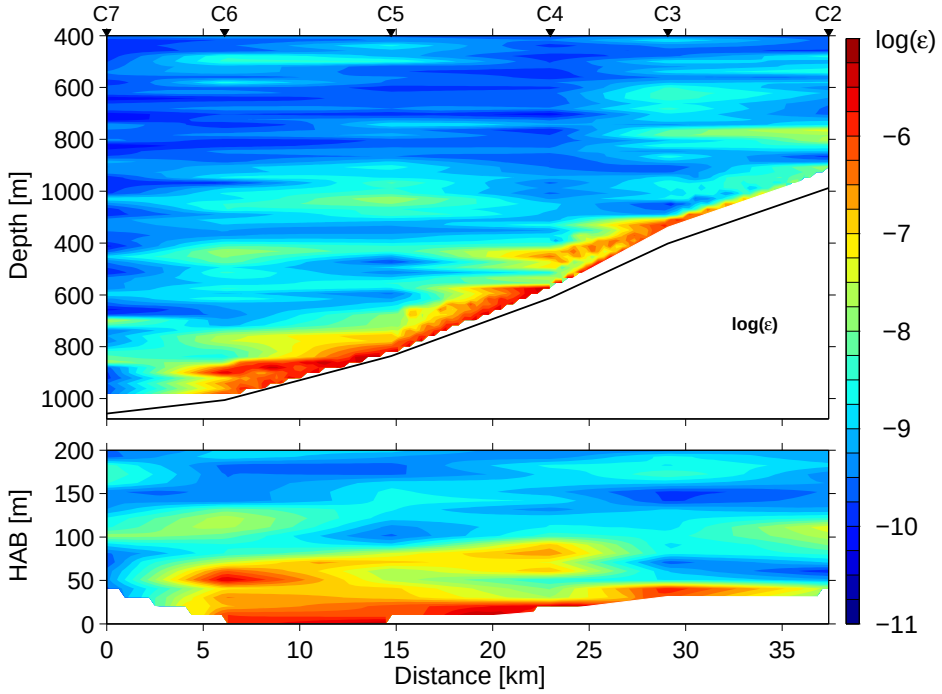

Figure 5.7: Same as Figure 5.6, but for section C.

sampling recirculating eddies. Thus also a screening criterion for minimum vertical velocity should be set.

Dissipation rate measurements are rejected when AOA is greater than 4.5° and 1.8° for dives and climbs, respectively. Similarly, criteria are set for vertical velocity W, leaving only data within $-35\,\mathrm{cm\,s^{-1}}$ to $-15\,\mathrm{cm\,s^{-1}}$ and $7\,\mathrm{cm\,s^{-1}}$ to $25\,\mathrm{cm\,s^{-1}}$ for dives and climbs, respectively.

To visualize the effect of the above rejection criteria, ensemble averages of all data, and different screenings of the data are shown in Figure 5.9, averaged in 10 m bins, and separated into dives and climbs. The upper left graph shows all data, which is also shown in faint colors in the other graphs for comparison. Screening with the criteria described above is applied in the upper right graph. Data below the 2nd percentile and above the 98th percentile for each 10 m bin are also rejected here, removing unreliably low or high data, such as the peak at around 300 m above bottom. The two middle graphs show screening for the vertical velocity ranges $|W| = 10\,\mathrm{cm\,s^{-1}}$ to $15\,\mathrm{cm\,s^{-1}}$ (left) and $|W| = 15\,\mathrm{cm\,s^{-1}}$ to $30\,\mathrm{cm\,s^{-1}}$ (right), while the bottom graphs are screened for AOA. The limits for dives are 0° to 3° and 3° to 4.5°, while the limits for climbs are lower, 0° to 1.5° and 1.5° to 2°. The profile screened for low-AOA is the most variable. With all screening criteria applied, the profile shows a steady increase in dissipation rates with depth, and the profile from dives agree well with the profile from climbs.

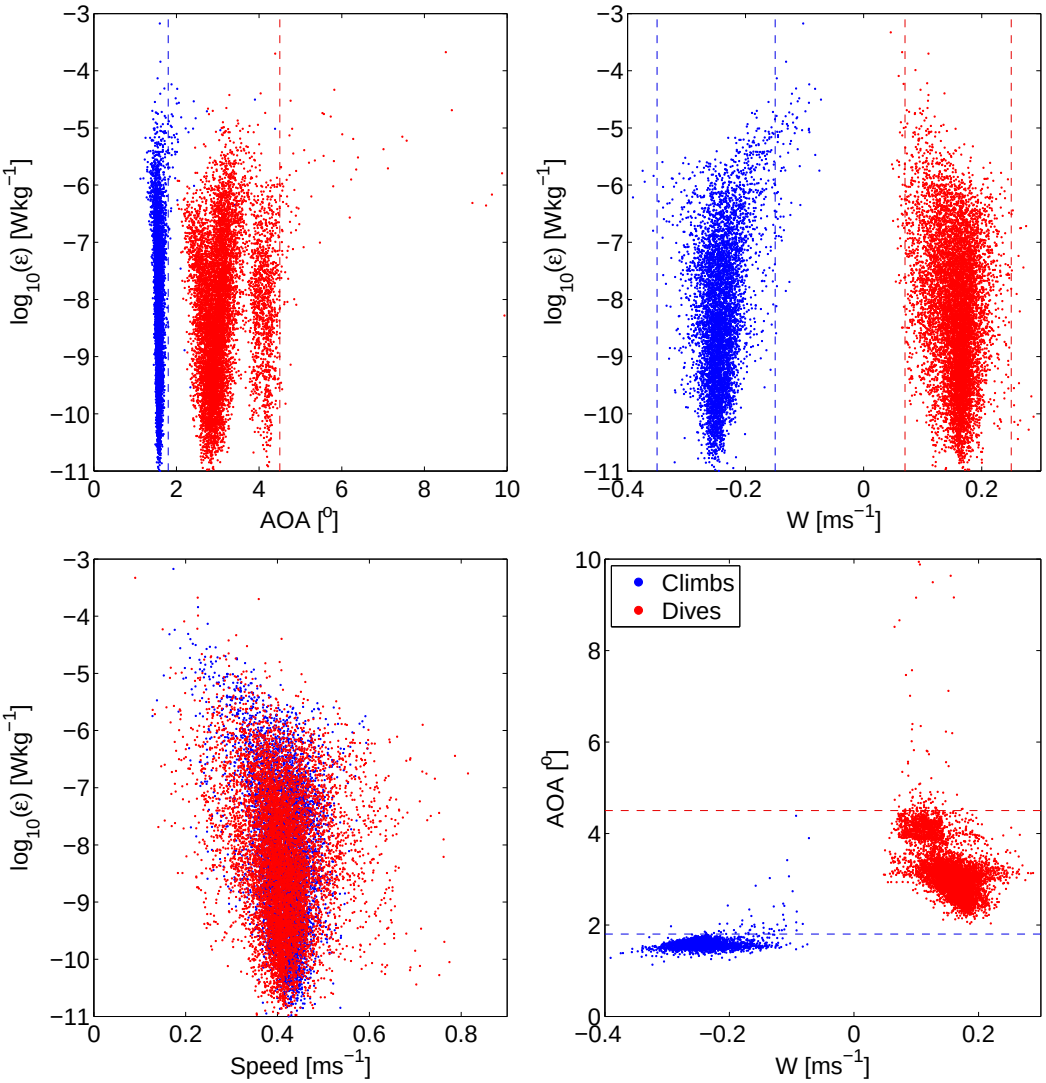

Figure 5.8: Scatterplots of navigational variables and shear-probe-derived dissipation, separated into dives (red) and climbs (blue). The graphs show angle of attack (AOA, upper left), vertical velocity (W, upper right) and speed (lower left) plotted against $\log_{10}(\varepsilon)$, and W against AOA (lower right). Rejection criteria are indicated with broken lines.

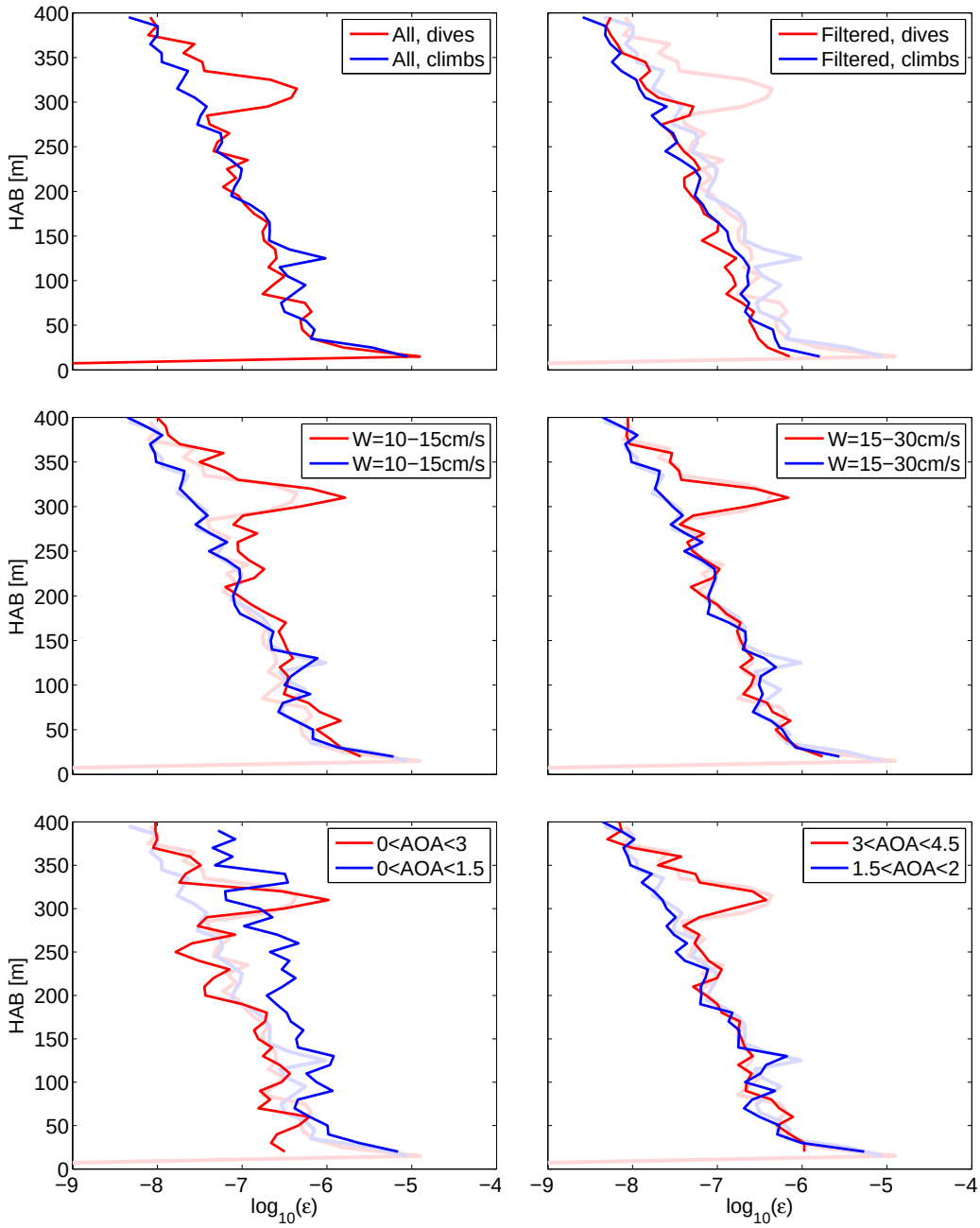

Figure 5.9: Ensemble average profiles of shear-probe derived $\log_{10}(\varepsilon)$, with respect to HAB, separated into dives (red) and climbs (blue). The upper left graph shows the profiles for all data, which are also shown in faint colors in all the other graphs. Upper right shows profiles using the limits indicated in Figure 5.8, and also removing data below/above the 2nd/98th percentiles, followed by two different screenings for vertical velocity (middle graphs) and two different screenings for AOA (lower graphs).

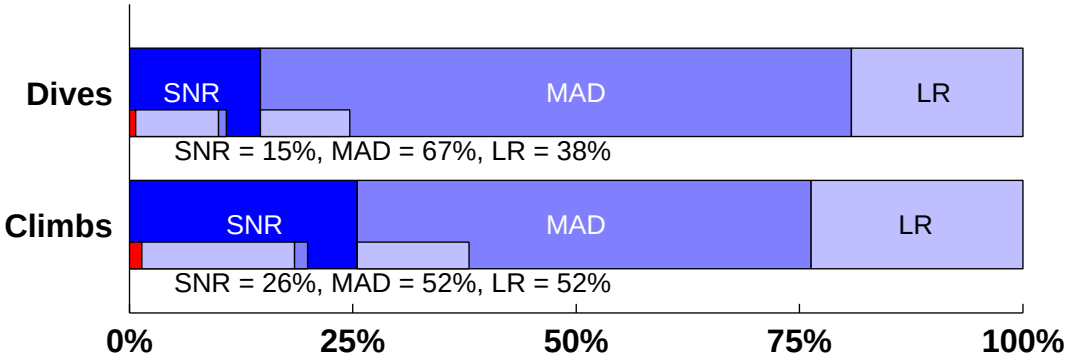

Figure 5.10: Distribution of the rejected Batchelor fit data segments. SNR is the signal to noise ratio, MAD is the mean absolute deviation, and LR is the $\log_{10}$(likelihood), as described in Section 3.3.1. The inserted bars shows how much the three criteria overlap, red insert bars show how much of the data were rejected by all three criteria.

5.2.2 Data screening: Maximum likelihood spectral fitting

Dissipation rate of TKE and temperature variance are calculated from the temperature gradient microstructure using the MLE spectral method outlined in Section 3.3.1. Following Ruddick et al. (2000), three criteria are applied to the MicroRider data to reject misfits and unreliable results, as described in Chapter 3. In total, 38 % and 28 % of the data were rejected from the dives and climbs, respectively. Figure 5.10 shows a summary of the distribution of rejected data segments, separated into dives and climbs. First, the signal-noise criterion (SNR) is displayed, followed by the mean absolute deviation (MAD) and finally the log_{10}(likelihood) ratio (LR) criteria. The small insert bars show how much of the SNR-rejected data are also rejected by MAD and LR, and how much of the MAD-rejected are also rejected by the LR criterion. The figures under the histograms show the relative percent rejected by each criterion, with MAD being the largest contributor, with 67 % for dives and 52 % for climbs. Only 0.7 % and 1.4 % of the rejected data satisfied all three criteria for dives and climbs, respectively, shown as red bars near 0 %.

5.2.3 Comparison of two methods

In order to compare the dissipation rates of TKE obtained using the two independent methods, data screening is applied, and profiles are survey-averaged in 10 m bins, relative to interface depth z_i, corresponding to the 3 °C isotherm. Shear-probe derived data are screened as described in Section 5.2.1. For MLE data, the three criteria described in Section 5.2.2, referred to as SNR, MAD and LR, are applied.

Survey average profiles Figure 5.11 shows survey-averaged profiles of VMP, shear probe-derived and MLE-derived dissipation rates, separated into dives and climbs, averaged in vertical with respect to interface depth (top) and to HAB (bottom). In order to exclude data from the bottom boundary layer in the interfacial profile, data within 25 m of the bottom are ignored in the average profile with respect

to the interface. The profiles show similar shape, with generally increasing dissipation rates closer to the bottom, where they approach $10^{-6}\,\mathrm{W\,m^{-2}}$. Seen relative to the interface depth, the shear-derived dissipation rates are systematically higher than VMP, and for the region above the interface depth this also applies to the MLE data. Between about 150 m to 300 m above bottom, the VMP values deviate from MLE and shear-derived, up to about a factor of four. Within 75 m above bottom, MLE estimates are significantly lower than shear-probe derived.

Histograms Histograms of TKE dissipation rates for each method, and at different depth segments are shown in Figure 5.12, and are compared to that obtained from the VMP. Dives and climbs are shown separately. The left column shows the results from the MLE method, and the right column shows results from the shear method. The upper row shows data in the range 50 m to 100 m above the interface depth, the middle row shows a 50 m range centered at the interface, and the bottom row shows 50 m to 100 m below the interface depth. Generally, VMP data shows lower dissipation rates than both the MLE and shear-derived methods, and particularly in the region above the interface. Below the interface, MLE dissipation rates are the lowest, consistent with Figure 5.11. Climbs show higher dissipation rates than dives, for both MLE and shear-derived measurements.

Similarly, Figure 5.13 compares all MLE (yellow) and shear-probe derived (green) data (dives and climbs together), in the same depth intervals as in Figure 5.12. VMP data are shown as black bars. MLE-derived dissipation rates are higher than the shear-derived above and at the interface, peaking at $10^{-8}\,\mathrm{W\,kg^{-1}}$. Below the interface, MLE-derived dissipation rates peak at one order of magnitude lower than the shear-derived. Above the interface, VMP generally shows lower dissipation rates than both MLE and shear. Both MLE and shear methods peak at $\varepsilon = 10^{-7}\,\mathrm{W\,kg^{-1}}$, while VMP dissipation rate distribution peaks at $10^{-8}\,\mathrm{W\,kg^{-1}}$. At, and below the interface, the VMP dissipation rate distribution is more in agreement with the glider-inferred distributions. Only the shear-derived dissipation rates exceed $10^{-5}\,\mathrm{W\,kg^{-1}}$, in the bottommost depth range.

5.3 Dissipation of TKE in the Faroe Bank Channel

Two glider sections are shown in Figure 5.14. The sections are color coded for dissipation rates ($\log_{10}(\varepsilon)$) on depth-time axes, found by interpolation of MLE-derived dissipation rates from the glider Gná. Isotherms for $T = 3, 6$ and 9 °C are shown as white contours for reference. The black lines zig-zagging the sections are the glider profiling tracks, and bathymetry is shown in gray. Above the two sections are maps showing the glider tracks, with the respective sections highlighted. The section in Figure 5.14d is downstream of the section in Figure 5.14c. The highly turbulent regions are mostly found along the bottom, but also at a height of about 200 m to 300 m above the bottom in some of the measurements, corresponding to the interfacial layer. In the downstream section (Figure 5.14d), the turbulent layer at the

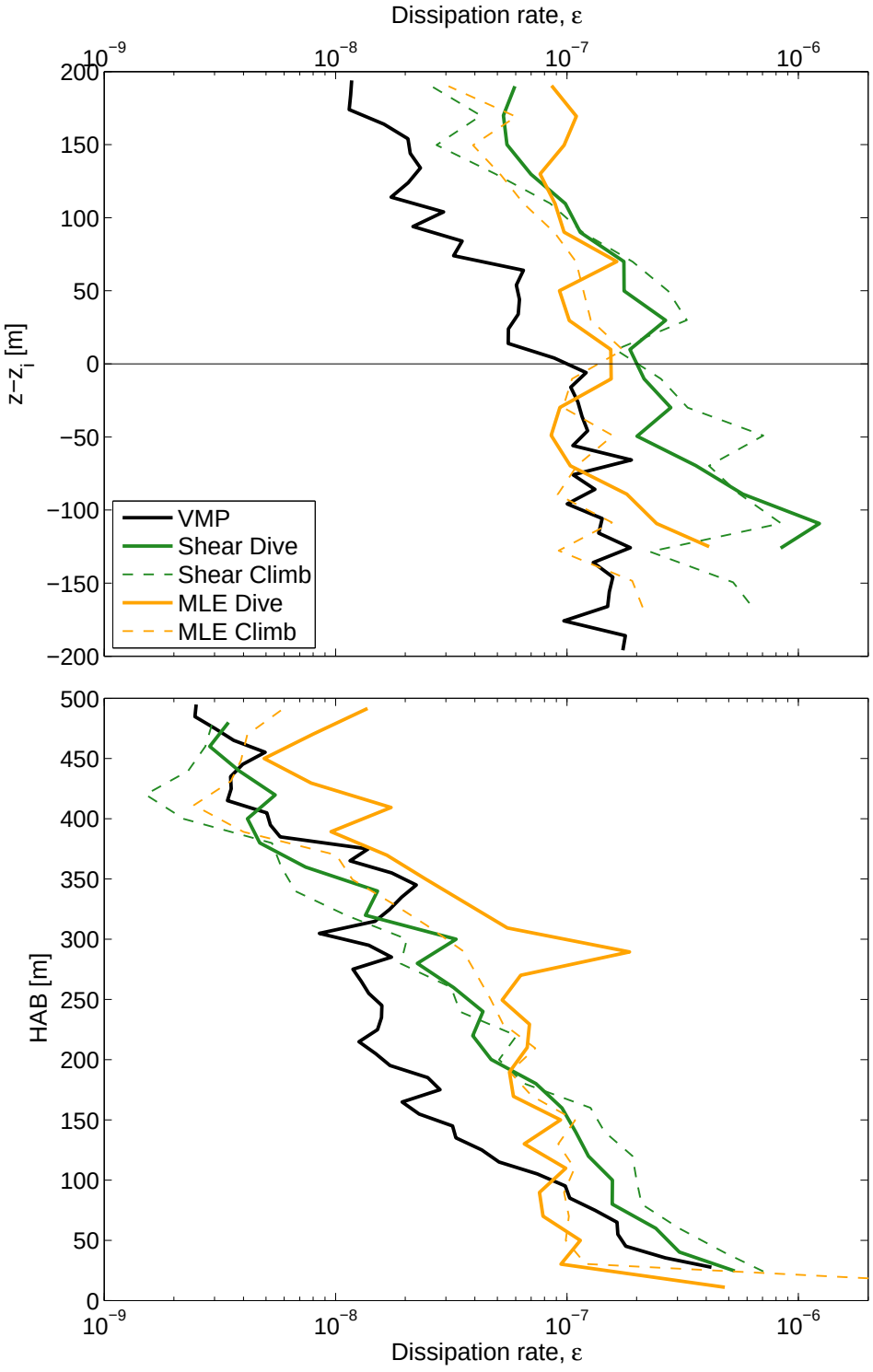

Figure 5.11: Survey-averaged profiles of dissipation of turbulent kinetic energy (ε) with respect to interface depth (z_i, top) and height above bottom (HAB, bottom). Profiles are derived from VMP casts (black), glider shear probes (green) and glider thermistors (yellow).

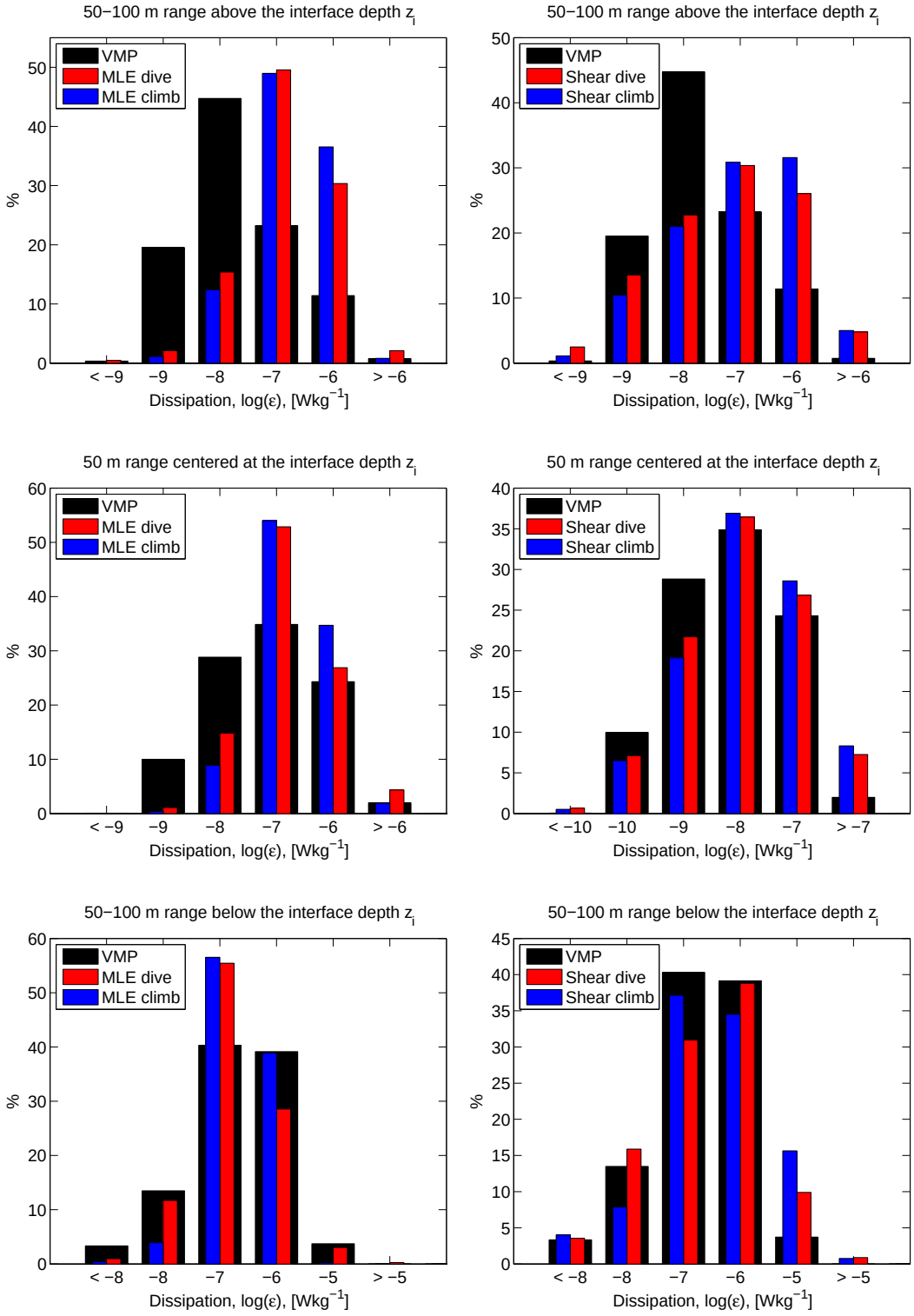

Figure 5.12: Histograms comparing the distribution of rate of dissipation of TKE, ε. VMP data are shown as black bars in all graphs. The left column of figures shows a comparison of MLE dives versus climbs, while the shear-derived dissipation is compared to the right. The figures investigate the ranges (top) 50 m to 100 m above the interface depth, (middle) 50 m range centered at the interface, and (bottom) 50 m to 100 m below the interface. Dives are shown as red bars, and climbs are shown as blue. Note the different scales on both axes.

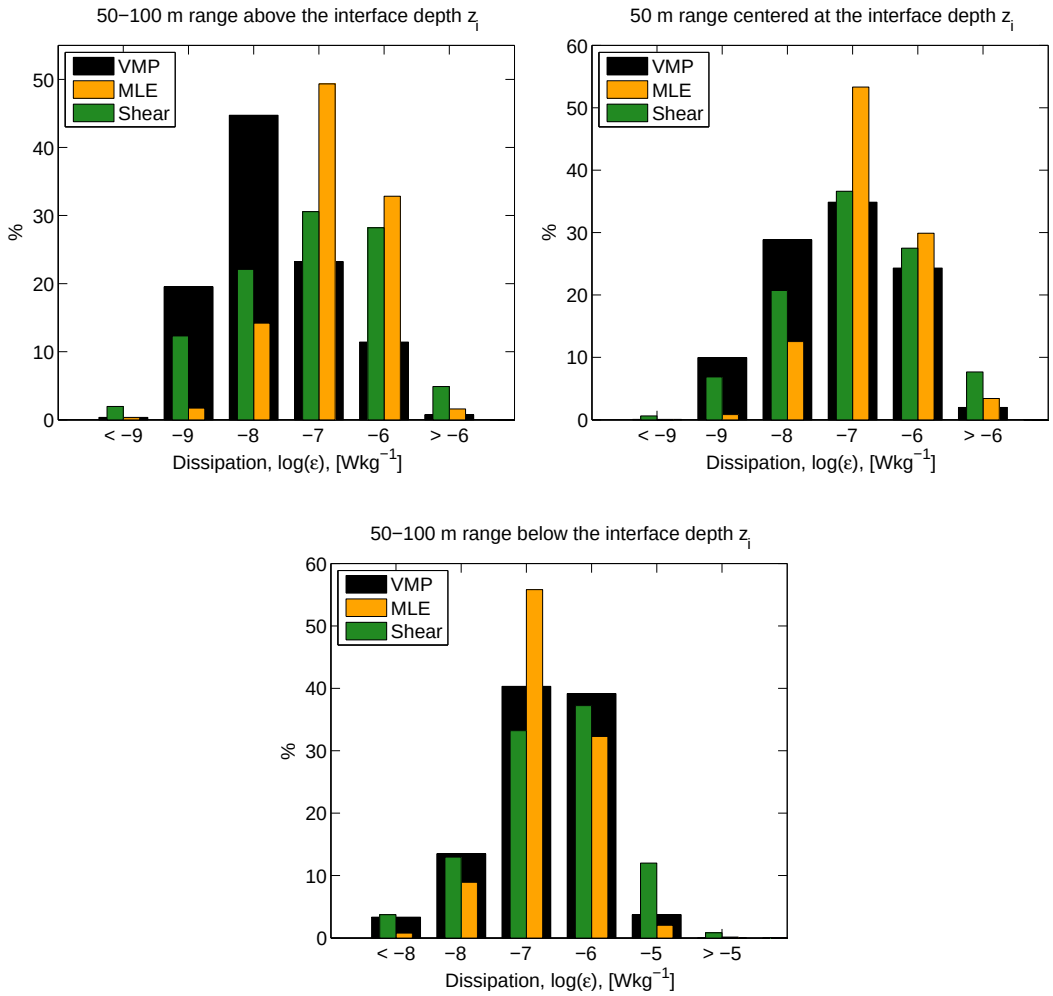

Figure 5.13: Same as Figure 5.12, but comparing MLE (yellow) to shear-derived (green). Upper left shows the range 50 m to 100 m above the interface, upper right at the interface, and bottom graph shows a the range 50 m to 100 m below the interface. Note the different scales on both axes.

bottom reaches higher, and the isotherms at 3 °C and 6 °C have a larger vertical separation than that in the upstream section (Figure 5.14c). The mid-depth range has higher dissipation rates in the downstream section than in the upstream, with more values in the $\varepsilon = 10^{-9}\,\mathrm{W\,kg^{-1}}$ to $10^{-8}\,\mathrm{W\,kg^{-1}}$ range (turquoise and green colors).

Depth-averaged dissipation rates are calculated for all dives and climbs reaching depths below 500 m, but the upper 100 m are excluded to avoid surface turbulence. Additionally, plume-integrated dissipation rates are calculated for all profiles with minimum temperature lower than 3 °C. Integration is done from the bottom and up to $H = 50\,\mathrm{m}$ above the 3 °C isotherm, $\rho_0 \int_0^H \varepsilon\, dz$. The integral is multiplied with a reference density of $1027.4\,\mathrm{kg\,m^{-3}}$ to give units of watts per square meter, following Beaird et al. (2012). The results are shown on the two maps in Figure 5.15, where each data point represents one depth-averaged profile (top) or one plume-integrated profile (bottom). For multiple occupations of a position, the higher values are plotted on top of the lower values. Relatively high values of averaged dissipation rates can be seen, in the path of the overflow plume at depths below 700 m, and further north,

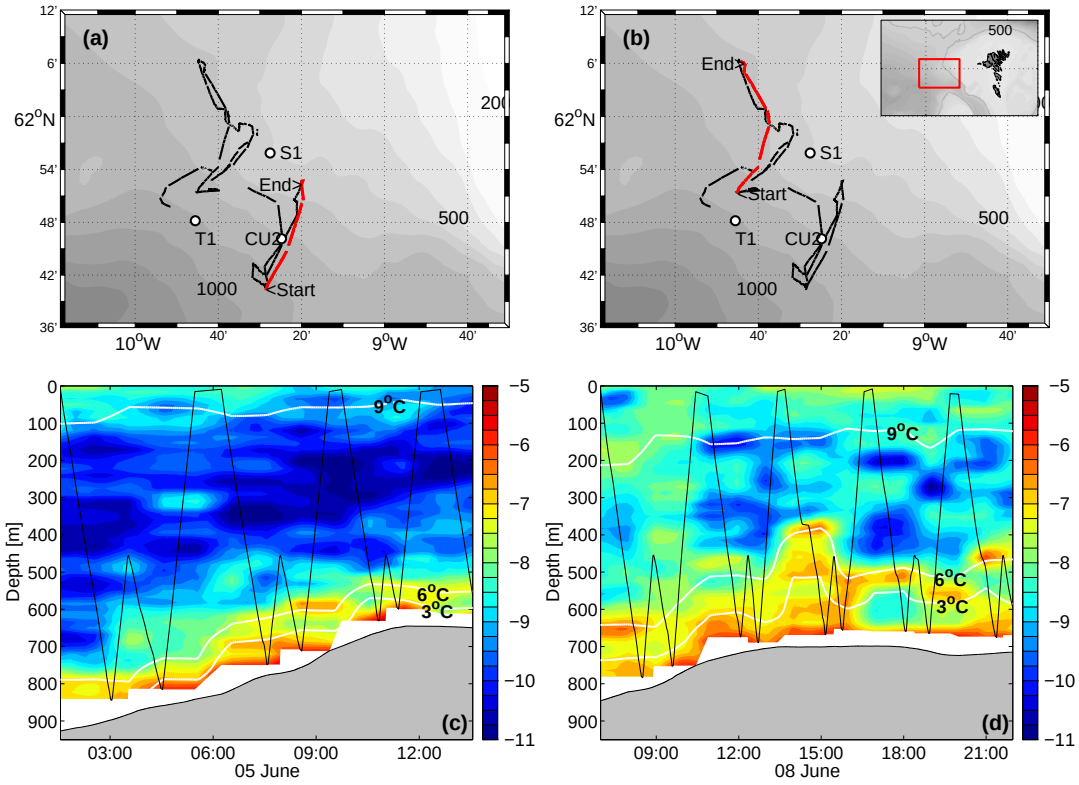

Figure 5.14: Bottom: Two sections from Gná's, color coded for the rate of dissipation of TKE, $\log_{10}(\varepsilon)$, with bathymetry in grey. Isotherms for $T = 3, 6$ and $9\,°\mathrm{C}$ are plotted as white contours. The glider tracks are shown in black. Top: Maps of the study area, marked with Gná's tracks, and the highlighted sections correspond to the figures below. The maps have depth contours every 100 m. The CTD/LADCP stations T1, S1 and CU2 are marked on the maps.

toward the Iceland-Faroe Ridge. Integrated dissipation rates are more scattered, values ranging from less than $1\,\mathrm{mW\,m^{-2}}$ and up to more than $1\,\mathrm{W\,m^{-2}}$ are seen in the overflow plume.

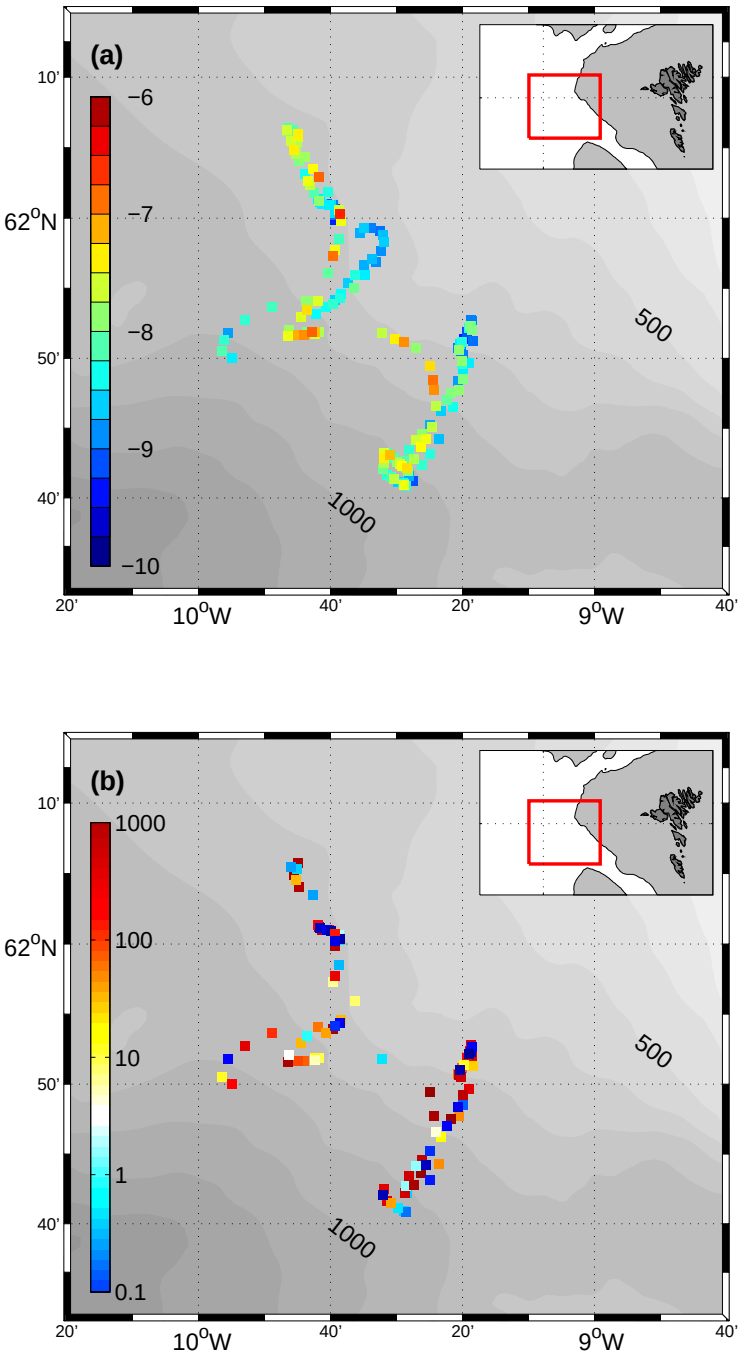

Figure 5.15: (a) Geometric depth averages of dissipation rates for depths below 100 m, where the color bar shows $\log_{10}(\varepsilon)$ in $\mathrm{W\,kg^{-1}}$, and (b) plume-integrated dissipation rates, $\rho_0 \int_0^H \varepsilon \, dz$, from the bottom to $H = 50$ m above the 3 °C isotherm. All Gná's profiles deeper than 500 m are included. The color bar in (b) has units of $\mathrm{mW\,m^{-2}}$. Depth contours are every 100 m, and depths less than 500 m are shaded in the insert maps.

Chapter 6

Discussion

6.1 Mixing studies with gliders

Gliders prove to be very useful in turbulence measurements. Since their propulsion does not rely on an engine or propeller, they provide a very low-vibration platform from which the MicroRider is capable of sampling dissipation rates of down to $10^{-11}\,\mathrm{W\,kg^{-1}}$. Using both shear probes and thermistors for turbulence measurements allows for two independent sampling methods from the same platform. Furthermore, indirect methods such as Thorpe scale overturn analysis can be used, which is not adressed in the present study. Because of the strong current in the plume, the gliders had trouble making cross-sections, and drifted downstream instead. During the one week of turbulence glider deployment in the FBC, a few useful sections were sampled. If specific cross-sections are required, the shipborne turbulence profilers (such as the VMP) are still more useful. In other areas, with less intense currents, this would not likely be a problem. For more extensive general surveying of ocean turbulence, the glider is an excellent platform, as it does not require much dedicated ship time, and multiple gliders may be deployed to sample simultaneously.

6.2 Sources of error

The glider measurements, and the calculations that finally lead to the dissipation rates of TKE, ε, require that several variables and constants are known. Some are well documented, and some are only partially known. The universal constant q is not accurately known, and the consequences of the choice of q are discussed below. This is followed by a discussion on the navigational variable angle of attack, upon which the calculated glider velocities critically depend.

6.2.1 The choice of q

The analytic form of the Batchelor spectrum (see Section 3.2.2) depends on the universal constant q, which is not well known. In this work, $q = 3.7$ is used, as was done by e.g. Nash et al. (1999). However, Bogucki et al. (2012) preferred the value

3.9, and Oakey (1982) calculated the value of q that gave the best fit for 16 separate spectra, finding values ranging from $q = 1.55$ to 6.95. The mean and standard deviation was $q = 3.7 \pm 1.5$, consistent with the findings of Grant et al. (1968), who found $q = 3.9 \pm 1.5$. In fact, q might even be a function of ε or the age of a patch, rather than a constant (Nash et al., 1999). Choosing the wrong value for q will lead to severe systematic errors in ε, because $\varepsilon \propto q^2$ (See Equations 3.7 and 3.11).

6.2.2 Angle of Attack

The angle of attack (AOA) is an important parameter for gliders, as both the velocity and the small scale shear estimates are very sensitive to this. In Figure 5.8 (upper left), AOA for dives appear in two clusters, at around 2.5° and 4°. The reason for this clustering is addressed by looking at time series of AOA, see Figure 6.1. The higher AOA values are associated with the second, shorter dive in a full W dive sequence. They are also related to lower vertical velocities (not shown). These two observations provide an explanation to the two clusters in AOA. Just after turning, at approximately 450 m in Figure 6.1, the glider has not had much time to accelerate before it meets the plume interface again. Its low momentum makes it more susceptible to the strong velocity shear at the interface of the plume. While the increased sampling in time and space allowed by the W-sampling scheme is desirable, the increased AOA cause reduced data quality in the turbulent interfacial layer. Such strongly sheared regions as the FBC overflow may be more accurately monitored with vertical profiling, although this requires more dedicated ship-time. For future deployments in strongly sheared flows, the high-AOA cluster may be avoided by using V-profiling instead of W-profiling. That way the glider surfaces between every dive, and will have enough momentum to penetrate into the plume.

Calculating the current velocity from shear probes assumes potential flow and small AOA, as discussed by Osborn and Crawford (1980). If the AOA is too large, the cross-stream velocity signal will be mixed with the downstream velocity fluctuations, so that the potential flow breaks down. The additional cross force due to viscous effects increase the cross force curve with increasing AOA. Also, the calibration tests by Osborn and Crawford (1980) show that the AOA should at least be kept below $\alpha = 20°$. The assumption of small AOA is fulfilled by the gliders, since even when including the high-AOA cluster angles rarely exceed 5°.

6.3 Shear-probe method

The shear-probe derived dissipation rates seem to be overestimated compared to those measured by the VMP, see Figure 5.11. A systematic offset is revealed in Figure 6.2, where the survey-averaged VMP and shear-derived dissipation rates are plotted relative to the interface depth (3 °C isotherm). Dividing the shear-derived dissipation rates by a factor 3 gives a good fit to VMP observations. Overestimates of the dissipation rates from the glider could be caused by the glider's slanted path,

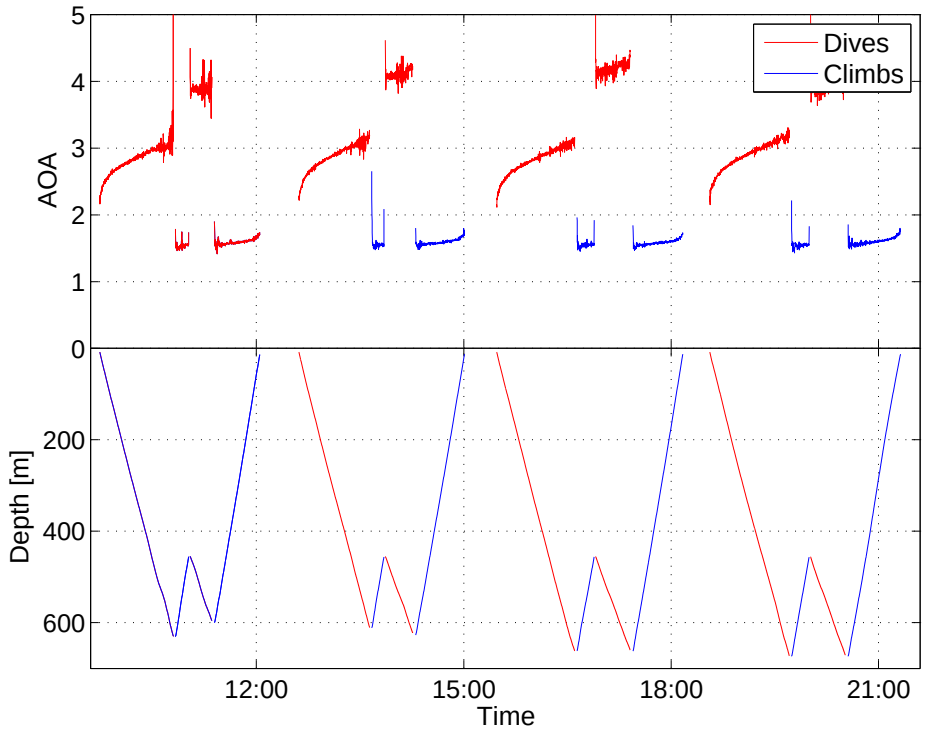

Figure 6.1: A sample from Gná's time series of AOA and depth.

which causes the glider to stay in turbulent regions for a longer duration, while the VMP, due to its mass can sink at a relatively constant rate of about $0.7\,\mathrm{m\,s^{-1}}$, penetrating through the overflow in an approximately vertical path. Since the glider will stay longer in such turbulent regions, it is more likely to capture mixing events, such as breaking of internal waves, which in turn will lead to overestimates of ε compared to that measured by VMP. The obstructing effect of turbulent regions on the glider can easily be seen (in the center of the section) in Figure 5.14b, where the glider track is clearly stalled on the way down through the turbulent (red) region at about 380 m depth.

A related issue is discussed by Thorpe (2012), who found that the glider's slanted path may lead to errors in the estimate of overturn scales, leading to an underestimate of ε by up to a factor of 2. The slanted path may also lead to observations of overturns (density inversions) that are not real. Note that turbulent overturn analysis is not done in this work, and this is of no concern here. However, Thorpe (2012), and the related numerical study by Smyth and Thorpe (2012), do not take in consideration the glider's motion caused by the background current, and they mention this to be a more relevant issue for strongly sheared oceanic flows, such as the FBC overflow. Smyth and Thorpe (2012) operate with a net velocity difference of $0.01\,\mathrm{m\,s^{-1}}$, while the velocity difference in the FBC is up to $1\,\mathrm{m\,s^{-1}}$.

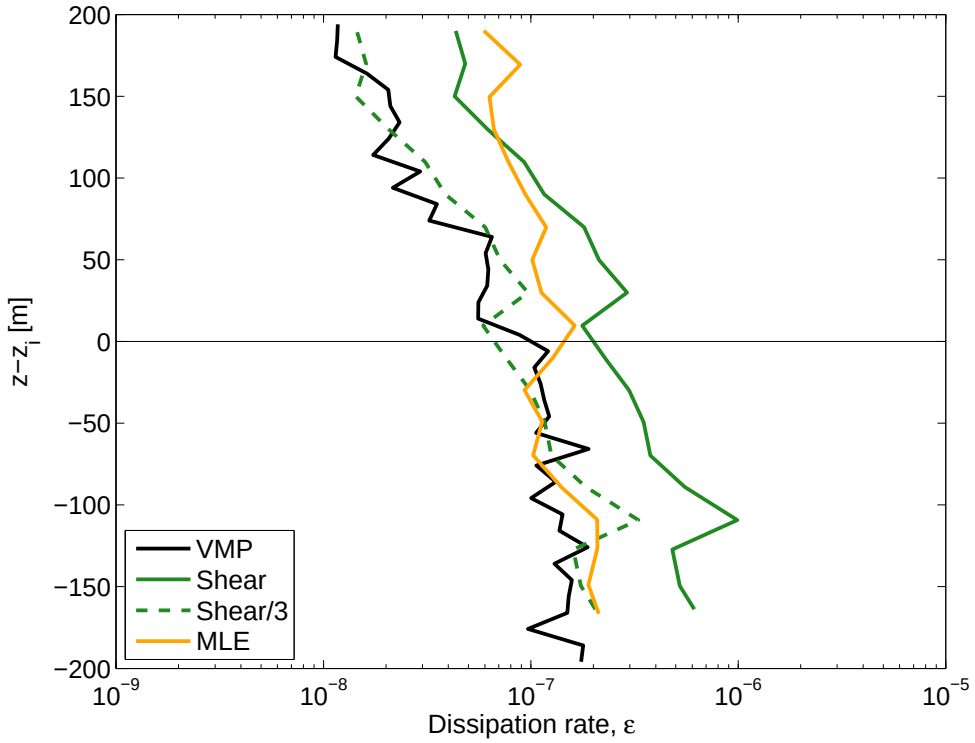

Figure 6.2: Survey-averaged profiles of VMP, shear- and MLE-derived $\log_{10}(\varepsilon)$, plus the shear-derived dissipation divided by a factor 3. Dives and climbs are combined.

6.4 Maximum likelihood estimate method

The maximum likelihood estimate method is described and evaluated by Ruddick et al. (2000). Using the same automated rejection criteria as in this study, described in Chapter 3, they rejected 22 % of the data segments, compared to 38 % and 28 % rejected dives and climbs, respectively, in this study. They found the $\log_{10}$(likelihood ratio) criteria to be the most effective for automated rejection, while in this study the mean absolute deviation (MAD) seems more effective, with up to 67 % of the rejected data being covered by this criterion. Signal-noise ratio is the least useful of the three, with only 5.3 % and 8.3 % of the rejected segments covered uniquely by this criterion. This is because sampling is done in a very turbulent environment with T-gradient spectra typically above the noise level.

In the bottommost part of the survey-averaged profile (Figure 5.11), the MLE method shows much lower values than the shear-probe derived. Sanchez et al. (2011) compared the spectral fit of the Batchelor (1959) model to the alternative model by Kraichnan (1968), and they found the latter to adjust better to their measured data. In particular, they found that the Batchelor fit underestimated the dissipation rate at high wave numbers. In the bottom layer of the present data set, dissipation rates are very large, and as the glider approach the bottom it moves into the high-wave number range, suggesting that the Batchelor estimates close to the bottom are underestimated. Any theoretical shape of the dissipation spectrum can be fitted in

the MLE method. In the present study, only the Batchelor form is utilized, and alternatives, such as the Kraichan, were not used due to the limited time period of the study. It is advisable to obtain independent estimates using both Kraichan and Batchelor spectral shapes.

6.5 Dissipation rates in the interior

The two sections in Figure 5.14 show different dissipation rates in the interior, between the surface layer and the top of the plume interface. The downstream section (d) has a more turbulent interior than the upstream (c), in many places about one order of magnitude higher dissipation rates. The downstream section (d) is located in the vicinity of "Mixing Zone 2" identified by Beaird et al. (2012).

Profiles of gradient Richardson number can be calculated from CTD and LADCP data, using Equation 2.6. The upstream section is well represented by CTD station CU2, both in time and space. For the downstream section no co-located CTD/LADCP stations are avaliable. Stations T1 and S1 are the closest, more than 10 km away from the section. Two profiles of Ri for 8 m intervals are shown in Figure 6.3, from stations T1 and CU2. Values of $\mathrm{Ri} < 1$ indicate that shear dominates over buoyancy, indicative of shear production and mixing. While theoretically $\mathrm{Ri} < 0.25$ is required, given the instrument resolutions and uncertainties involved in Ri calculations, $\mathrm{Ri} < 1$ is typically considered indicative of shear instability. The FBC region has a two-layered flow pattern, with outflow at the bottom, and inflow above. This current shear could lead to mixing even in the interior. These profiles reveal equal fractions of $\mathrm{Ri} < 1$ in the interior, between 100 m to 500 m depth, of 28 %. However, by investigation of subsequent profiles in T1 and CU2, 1 h to 6 h apart, respectively, great temporal variability is revealed. Five subsequent profiles of T1 and two profiles of CU2 show variation in percent $\mathrm{Ri} < 1$ in the interior ranging from 28 % to 46 %. The spatial and temporal coverage by CTD and LADCP is to low to determine the cause of the elevated dissipation rates in the section. The tides in the Faroe Bank Channel are strong, dominated by the M2 component. Mauritzen et al. (2005) suggest that the channel may be a site of tide-forced, resonant internal waves, which could induce strong mixing. In lack of evidence opposing the glider-derived observations, the difference in dissipation rates between the two sections is regarded to be the true nature of the flow, rather than observational errors.

6.6 Comparison of methods

6.6.1 Chi-square test

A chi-square test is used to determine whether two measured data sets come from the same distribution. The theory behind the test is described in Section 3.3.2. The null hypothesis claims that two data sets come from the same, unspecified distribution. The data used for the histograms in Figure 5.12 were tested for the null hypothesis,

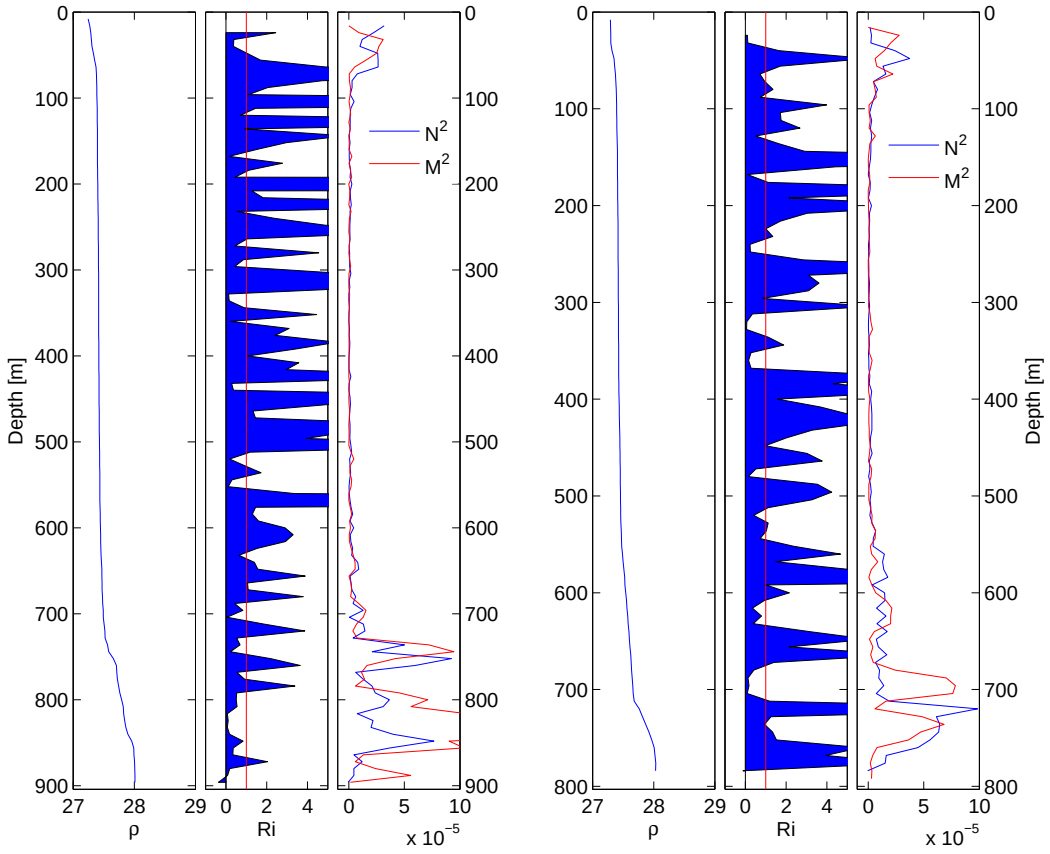

Figure 6.3: Profiles of density, Richardson number using 8 m intervals, shear ($M^2 = (\partial u/\partial z)^2 + (\partial v/\partial z)^2$) and buoyancy frequency ($N^2 = -g/\rho_0 \times \partial\rho/\partial z$), for stations T1 and CU2 (see Figure 4.6. Both these two profiles have 28 % Ri < 1 between 100 m to 500 m depth.

comparing MLE-derived dissipation rates to VMP-derived. This was done separately for the three 50 m depth ranges relative to the interface depth, which was also used for the histograms. The null hypothesis was rejected for the segments above and at the interface, which indicates that the data are sampled from different distributions. Below the interface, however, the null hypothesis was not rejected, indicating that the data are likely to come from the same distribution. The results of the test is sensitive to number of bins, and these results were obtained with 300 bins, a reasonable choice for the large number of data points involved.

Tables 6.1 and 6.2 show the maximum likelihood estimated (see Section 3.3.1) mean and 95 % confidence intervals of the data sets used in Figures 5.12 and 5.13, respectively.

6.6.2 Fitting a probability distribution function

There is a possibility that the expected mean values of the observed data (Table 6.2) are contaminated by noise in the low and high dissipation rate ranges, caused by e.g.

Table 6.1: Mean and 95 % lower and upper confidence limits from lognormal distribution for data from three 50 m depth ranges; above, at and below the interface depth. The columns represent calculations for VMP data, temperature-derived (Batchelor) data and shear-derived (Nasmyth) data. Glider data is separated into dives and climbs. Units for rate of dissipation of turbulent kinetic energy are $\mathrm{W\,kg^{-1}}$, and all numbers are multiplied with 10^7 here for comparison.

(a) $10^7 \times \varepsilon$, 50 m to 100 m above the interface depth.

$[\mathrm{W\,kg^{-1}}]$	VMP	Batchelor		Nasmyth	
		Dives	*Climbs*	*Dives*	*Climbs*
Mean	0.5	2.1	1.6	6.7	6.7
Low	0.4	1.9	1.4	5.2	5.1
Up	0.7	2.5	1.8	8.6	8.9

(b) $10^7 \times \varepsilon$, 50 m range centered at the interface depth.

$[\mathrm{W\,kg^{-1}}]$	VMP	Batchelor		Nasmyth	
		Dives	*Climbs*	*Dives*	*Climbs*
Mean	2.2	1.9	1.7	5.9	6.8
Low	1.8	1.7	1.6	4.9	5.3
Up	2.7	2.2	2.0	7.2	8.8

(c) $10^7 \times \varepsilon$, 50 m to 100 m below the interface depth.

$[\mathrm{W\,kg^{-1}}]$	VMP	Batchelor		Nasmyth	
		Dives	*Climbs*	*Dives*	*Climbs*
Mean	3.5	1.7	1.3	9.8	15.0
Low	2.8	1.4	1.7	7.7	10.7
Up	4.4	1.9	1.5	12.6	21.0

motion of the sensor platform, or excessive correction for shear-derived dissipation rates. Observed dissipation rates of TKE ($\log_{10}(\varepsilon)$) can be transformed into a probability density function (PDF), by separating the data into bins and dividing by the integral value, such that the area under the graph is unity. Assume that the dissipation rates from VMP lower than $3 \times 10^{-10}\,\mathrm{W\,m^{-2}}$ are dominated by noise. Similarly, it can be assumed that the glider has a noise level of $3 \times 10^{-10}\,\mathrm{W\,m^{-2}}$, and also that dissipation rates greater than $10^{-6}\,\mathrm{W\,m^{-2}}$ are likely to suffer from oversampling and high AOA. The selected part above the assumed noise level, and in the glider case, below the assumed oversampling limit, can be fitted by a log-normal PDF. In Figure 6.4 such fits are made, continuing to use the 50 m depth segments relative to the interface depth as in Figure 5.13. The figure shows the raw PDFs, and the part used for PDF fits are highlighted, overlain by the normal PDF fit. Vertical lines show the expected mean values of the raw data (solid line), a fitted PDF to all bins (dashed line, PDF is not shown), and the fitted PDF to selected bins (thick line). The expected mean values of the raw data are calculated by MLE, as described in Section 3.3.1, and given in Table 6.2. For the fitted PDFs, the expected values are

Table 6.2: Same calculations as in Table 6.1, covering three 50 m depth ranges; above, at and below the interface depth, but using dive and climb data combined.

(a) $10^7 \times \varepsilon$, 50 m to 100 m above the interface depth.

[W kg^{-1}]	VMP	Batchelor	Nasmyth
Mean	0.5	1.9	6.8
Low	0.4	1.7	5.6
Up	0.7	2.1	8.2

(b) $10^7 \times \varepsilon$, 50 m range centered at the interface depth.

[W kg^{-1}]	VMP	Batchelor	Nasmyth
Mean	2.2	1.9	6.3
Low	1.8	1.7	5.4
Up	2.7	2.0	7.3

(c) $10^7 \times \varepsilon$, 50 m to 100 m below the interface depth.

[W kg^{-1}]	VMP	Batchelor	Nasmyth
Mean	3.5	1.6	11.6
Low	2.8	1.4	9.5
Up	4.4	1.7	14.2

calculated from Equation 3.23. The calculated values are shown in Table 6.3.

Expected mean values for Nasmyth at, and below the interface are significantly lowered using the selected fit, compared to the fit over all bins. Above the interface, expected Nasmyth value is increased by a factor of 2 for the fitted data. At the interface, the expected value for Batchelor data is significantly reduced for PDF fits, while the reduction is more slight above and below the interface. Overall, the PDFs at and below the interface depth range seem to agree somewhat on the distribution, although the standard deviation of the shear-derived Nasmyth and VMP distributions are greater than that of the PDF of Batchelor-derived data, which caused it to be rejected by the chi-square test in Section 5.2.3. Above the interface, however, the agreement between glider-derived and VMP dissipation rates remains inadequate.

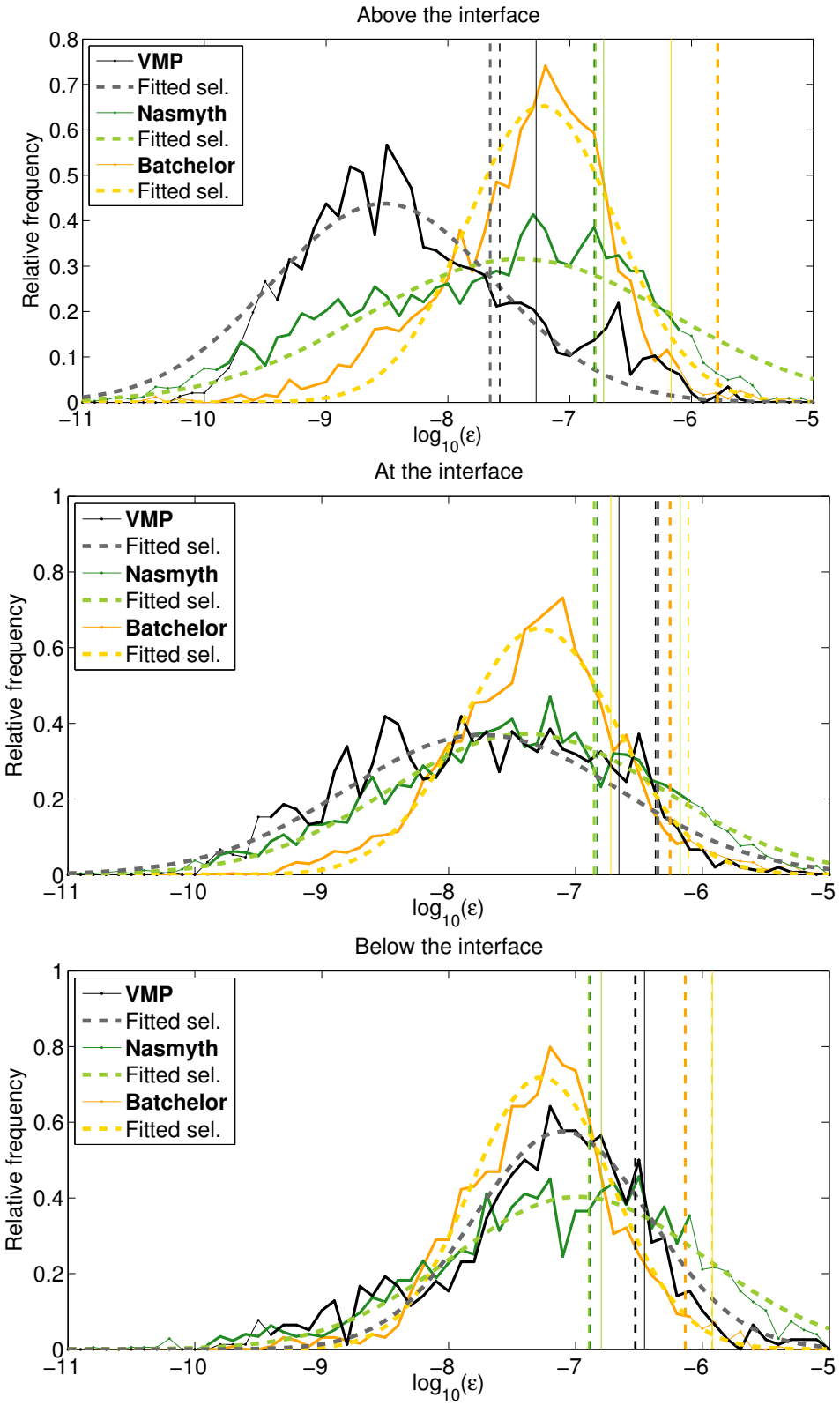

Figure 6.4: Relative frequency of occurences, and the fitted probability distribution functions (PDFs). The highlighted parts of each frequency graph shows what is included in each PDF. The vertical lines show the expected mean of the calculated MLE (thin, solid), fitted PDF when all data were considered (thin, dashed), and the fitted PDF when high and low values were ignored (thick), see Table 6.3 for values.

Table 6.3: Expected mean values of the lognormal distributions. Values in "All data" row is calculated using MLE calculations directly on the data, from Table 6.2. "All fitted" values is the expected value calculated using Equation 3.23, by fitting a log-normal PDF on normalized histogram of all the data, and "Selected fit." shows the result from fits where noise and oversampling are excluded. The calculations are for the three 50 m depth ranges; above, at and below the interface depth. All numbers are multiplied with 10^7 here for comparison.

(a) $10^7 \times \varepsilon$, 50 m to 100 m above the interface depth.

$[\mathrm{W\,kg^{-1}}]$	VMP	Batchelor	Nasmyth
All data	0.5	1.9	6.8
All fitted	0.3	1.6	16.1
Selected fit.	0.2	1.6	16.5

(b) $10^7 \times \varepsilon$, 50 m range centered at the interface depth.

$[\mathrm{W\,kg^{-1}}]$	VMP	Batchelor	Nasmyth
All data	2.2	6.7	1.9
All fitted	4.3	1.5	7.7
Selected fit.	4.5	1.4	4.9

(c) $10^7 \times \varepsilon$, 50 m to 100 m below the interface depth.

$[\mathrm{W\,kg^{-1}}]$	VMP	Batchelor	Nasmyth
All data	3.5	1.6	12.0
All fitted	3.0	1.3	11.9
Selected fit.	3.0	1.3	7.1

Chapter 7

Concluding remarks

The application of turbulence instrumentation on underwater gliders is addressed, and two methods for glider-inferred dissipation rates of turbulent kinetic energy (TKE) are evaluated against a ship-based vertical microstructure profiler (VMP). The VMP is a well established method for acquiring dissipation rates, and is used as a reference for the two other methods. One glider equipped with microstructure sensors for velocity shear and temperature was deployed in the Faroe Bank Channel Overflow in June 2012. The site is the deepest of two main connections across the Greenland-Iceland-Scotland ridge. Along the bottom of the channel, a plume of cold, dense water flows from the Nordic Seas into the North Atlantic. The interface between the plume and the ambient is strongly sheared, and severe mixing takes place there.

High resolution vertical profiles of velocity shear are used to calculate dissipation rates. This is done by integrating the wavenumber spectrum, which is fitted to the Nasmyth universal spectrum. Unreliable data are filtered out by screening of navigational variables, such as angle of attack, vertical and horizontal velocities. Survey averages were made with 10 m vertical bin averaging with respect to plume interface depth, and to height above bottom. Generally, the survey-averaged profiles of the glider's shear-derived dissipation rates resemble those measured by the VMP, with increasing dissipation rates towards the interface and the bottom. Shear-derived dissipation rates suffer from an offset in the highly sheared interface region by a factor 3 compared to that derived from VMP. The glider velocity is not measured directly, and its calculation is very sensitive to the angle of attack, which is also not measured directly, but must be estimated from other navigational parameters.

Variance in temperature microstructure provides another method to calculate dissipation rates. Temperature gradient spectra are fitted to the universal Batchelor form using the maximum likelihood estimate (MLE). The dissipation rate of turbulent kinetic energy (ε) and the rate of dissipation of thermal variance (χ_θ) can be calculated by using the maximum likelihood estimate fit to the temperature gradient spectrum. Three criteria for automated rejection of bad data segments are used, concerning signal to noise ratio, mean average deviation (MAD), and log-likelihood ratio. The MAD criterion is found to be the most effective in this data set, identify-

ing 67 % and 52 % of the rejected data segments from dives and climbs, respectively. Survey-averaged profiles of MLE-derived ε also compare reasonably well to VMP, but seems to underestimate dissipation rates at high wave numbers, close to the bottom, a caveat that was also identified by Sanchez et al. (2011). A chi square test on the VMP-derived ε versus the MLE-derived dissipation rate distributions indicate that they are sampled from the same distribution in a segment below the interface. For segments at- and above the interface, the discrepancies are too large to be accepted by the chi-squared test.

The MLE method should also be applied by fitting the Kraichan universal spectrum, to reveal differences in dissipation rates inferred through the Batchelor spectrum, and possibly improve the estimates of dissipation rates of turbulent kinetic energy. In order to improve the accuracy of dissipation rates inferred through Batchelor spectral form, the value of q should be further investigated. In future work, high AOA experienced during dives can be lowered by applying full V-profiling instead of W-profiling, as dives starting at the surface could easier penetrate the plume. A dedicated flight model of the glider equipped with a MicroRider to infer more accurate AOA can further reduce the uncertainties. Errors due to flow distortion could be investigated in detail by expanding the model of Wyngaard et al. (1985) to a Slocum glider equipped with MircoRider, to see whether they in fact are negligible.

Overall, measurement of dissipation rates from gliders is a powerful addition to traditional shipborne turbulence profilers, as they make it possible to survey large areas by deploying several gliders. Measurements are reasonably accurate, and require much less dedicated ship time.

Bibliography

Baines, P. G. (1995), *Topographic Effects in Stratified Flows*, Cambridge University Press.

Baker, M. and Gibson, C. (1986), 'Sampling turbulence in the stratified ocean: Statistical consequences of strong intermittency', *Journal of Physical Oceanography* **17**, 1817 – 1836.

Batchelor, G. K. (1959), 'Small-scale variation of convected quantities like temperature in turbulent fluid. Part 1: General discussion and the case of small conductivity', *Journal of Fluid Mechanics* **5**(1), 113–133.

Beaird, N., Fer, I., Rhines, P. and Eriksen, C. (2012), 'Dissipation of turbulent kinetic energy inferred from seagliders: An application to the eastern Nordic Seas overflows', *Journal of Physical Oceanography* **42**, 2268 – 2282.

Bogucki, D., Luo, H. and Domaradzki, J. (2012), 'Experimental evidence of the Kraichnan scalar spectrum at high Reynolds number', *Journal of Physical Oceanography* **42**, 1717–1728.

Borenäs, K. M. and Lundberg, P. A. (1988), 'On the deep-water flow through the Faroe Bank Channel', *Journal of Geophysical Research* **93**(C2), 1281–1292.

Brandon, M. A., Cottier, F. R. and Nilsen, F. (2009), *Sea Ice*, Wiley-Blackwell, chapter 3, pp. 79 – 111.

Coachman, L. K. and Aagaard, K. (1988), 'Transports through Bering Strait - Annual and interannual variability', *Journal of Geophysical Research* **93**(C12), 15535–15539.

Cushman-Roisin, B. and Beckers, J.-M. (2011), *Introduction To Geophysical Fluid Dynamics - Physical and Numerical Aspects*, 2 edn, Acade.

Dooley, H. and Meincke, J. (1981), 'Circulation and water masses in the Faroese Channels during overflow '73', *Ocean Dynamics* **34**(2), 41–55.

Emery, W. and Thomson, R. (2001), *Data Analysis Methods in Physical Oceanography*, 2 edn, Elsevier.

Fer, I. and Paskyabi, M. (2013), 'Autonomous ocean turbulence measurements with a moored instrument', *Submitted* .

Fer, I., Voet, G., Seim, K. S., Rudels, B. and Latarius, K. (2010), 'Intense mixing of the Faroe Bank Channel overflow', *Geophysical Research Letters* **37**, L02604.

Garau, B., Ruiz, S., Zhang, W., Pascual, A., Heslop, E., Kerfoot, J. and Tintoré, J. (2011), 'Thermal lag correction on Slocum CTD glider data', *Journal of Atmospheric and Oceanic Technology* **28**, 1065 – 1071.

Girton, J. B., Pratt, L. J., Sutherland, D. A. and Price, J. F. (2006), 'Is the Faroe Bank Channel overflow hydraulically controlled?', *Journal of Physical Oceanography* **36**(12), 2340–2349.

Girton, J. B. and Sanford, T. B. (2003), 'Descent and modification of the overflow plume in the Denmark Strait', *Journal of Physical Oceanography* **33**(7), 1351–1364.

Grant, H. L., Hughes, B. A., Vogel, W. M. and Moilliet, A. (1968), 'Spectrum of temperature fluctuations in turbulent flow', *Journal of Fluid Mechanics* **34**, 423–442.

Gregg, M. and Meagher, T. (1980), 'The dynamic response of glass rod thermistors', *Journal of Geophysical Research* **85**, 2779 – 2786.

Hansen, B. and Østerhus, S. (2000), 'North Atlantic-Nordic Seas exchanges', *Progress In Oceanography* **45**(2), 109–208.

Hansen, B. and Østerhus, S. (2007), 'Faroe Bank Channel overflow 1995-2005', *Progress In Oceanography* **75**(4), 817–856.

Hogg, R. and Tanis, E. (2010), *Probability and Statistical inference*, Pearson Education Inc.

Johnson, G. C. and Sanford, T. B. (1992), 'Secondary circulation in the Faroe Bank Channel outflow', *Journal of Physical Oceanography* **22**(8), 927–933.

Jones, C., Creed, E., Glenn, S., Kerfoot, J., Kohut, J., Mudgal, C. and Schofield, O. (2005), Slocum gliders - A component of operational oceanography, *in* 'Proceedings of 14th International Symposium on Unmanned Untethered Submersible Technology (UUST)'.

Kraichnan, R. (1968), 'Small-scale structure of a scalar field convected by turbulence', *Physics of Fluids* **11**(5), 945–953.

Mauritzen, C., Price, J., Sanford, T. and Torres, D. (2005), 'Circulation and mixing in the Faroese Channels', *Deep-sea Research* **52**(6), 883–913.

McDougall, T. and Barker, P. (2011), *Getting started with TEOS-10 and the Gibbs Seawater (GSW) Oceanographic Toolbox*, SCOR/IAPSO WG127.

Merckelbach, L., Smeed, D. and Griffiths, G. (2010), 'Vertical water velocities from underwater gliders', *Journal of Atmospheric and Oceanic Technology* **27**, 547 – 563.

Nash, J., Caldwell, D., Zelman, M. and Moum, J. (1999), 'A thermocouple probe for high-speed temperature measurement in the ocean', *Journal of Atmospheric and Oceanic Technology* **16**, 1474 – 1482.

Nash, J. D., Peters, H., Kelly, S. M., Pelegri, J. L., Emelianov, M. and Gasser, M. (2012), 'Turbulence and high-frequency variability in a deep gravity current outflow', *Geophysical Research Letters* **39**, L18611.

Nasmyth, P. (1970), Oceanic turbulence, PhD thesis, University of British Columbia.

Oakey, N. (1982), 'Determination of the rate of dissipation of turbulent energy from simultaneous temperature and velocity shear microstructure measurements', *Journal of Physical Oceanography* **12**, 256 – 271.

Osborn, T. and Crawford, W. (1980), *Air-Sea Interaction, Instruments and methods*, Springer, chapter 19, pp. 369 – 386.

Osborn, T. and Lueck, R. (1985), 'Turbulence measurements with a submarine', *Journal of Physical Oceanography* **15**, 1502 – 1520.

Pratt, L. and Helfrich, K. (2005), 'Generalized conditions for hydraulic criticality of oceanic overflows', *Journal of Physical Oceanography* **35**(10), 1782–1800.

Pratt, L. J. (1986), 'Hydraulic control of sill flow with bottom friction', *Journal of Physical Oceanography* **16**(11), 1970–1980.

Press, W., Teukolsky, S., Vetterling, W. and Flannery, B. (1992), *Numerical Recipes in Fortran - The Art of Scientific Computing*, Cambridge University Press, chapter 14, pp. 614 – 617.

Ruddick, B., Anis, A. and Thompson, K. (2000), 'Maximum likelihood spectral fitting: The Batchelor spectrum', *Journal of Atmospheric and Oceanic Technology* **17**(11), 1541–1555.

Sanchez, X., Roget, E., Planella, J. and Forcat, F. (2011), 'Small-scale spectrum of a scalar field in water: The Batchelor and Kraichman models', *Journal of Physical Oceanography* **41**, 2155 – 2167.

Saunders, P. M. (1990), 'Cold outflow from the Faroe Bank Channel', *Journal of Physical Oceanography* **20**(1), 29–43.

Saunders, P. M. (2001), *Ocean circulation & climate*, Vol. 77, Academic Press, chapter 5.6: The dense northern overflows, pp. 401–417.

Seim, K. S. and Fer, I. (2011), 'Mixing in the stratified interface of the Faroe Bank Channel overflow: The role of transverse circulation and internal waves', *Journal of Geophysical Research* **116**(C07), C07022.

Seim, K. S., Fer, I. and Berntsen, J. (2010), 'Regional simulations of the Faroe Bank Channel overflow using a sigma-coordinate ocean model', *Ocean Modelling* **35**(1-2), 31–44.

Sirevaag, A. and Fer, I. (2012), 'Vertical heat transfer in the Arctic Ocean: The role of double-diffusive mixing', *Journal of Geophysical Research* **117**, C07010.

Slocum Glider Data Sheet (2010). Teledyne Webb Research.
URL: *http://www.webbresearch.com/pdf/Slocum_Glider_Data_Sheet.pdf*

Slocum Glider Operators Manual (2011). Teledyne Webb Research.

Smyth, W. and Thorpe, S. A. (2012), 'Glider measurements of overturning in a Kelvin-Helmholtz billow train', *Journal of Marine Research* **70**, 119–140.

Swift, J. H. (1984), 'The circulation of the Denmark Strait and Iceland Scotland overflow waters in the North-Atlantic', *Deep-sea Research* **31**(11), 1339–1355.

Swift, J. H., Aagaard, K. and Malmberg, S.-A. (1980), 'The contribution of the Denmark Strait overflow to the deep North Atlantic', *Deep Sea Research* **27**(1), 29–42.

Taylor, G. (1935), Statistical theory of turbulence, *in* 'Proceedings of the Royal Society of London A: Mathematical and Physical Sciences', The Royal Society.

Thorpe, S. A. (2005), *The Turbulent Ocean*, Cambridge University Press.

Thorpe, S. A. (2007), *An Introduction to Ocean Turbulence*, Cambridge University Press.

Thorpe, S. A. (2012), 'Measuring overturns with gliders', *Journal of Marine Research* **70**, 93–117.

Turner, J. S. (1973), *Buoyancy Effects in Fluids*, Cambridge University Press.

Umlauf, L. and Arneborg, L. (2009), 'Dynamics of rotating shallow gravity currents passing through a channel. Part II: Analysis', *Journal of Physical Oceanography* **39**(10), 2402–2416.

Wolk, F., Lueck, R. and St. Laurent, L. (2009), Turbulence measurements from a glider, *in* 'Marine Technology for Our Future: Global and Local Challenges', MTS/IEEE, MTS/IEEE, pp. 1 – 6.

Wolk, F., Yamazaki, H., Seuront, L. and Lueck, R. G. (2002), 'A new free-fall profiler for measuring biophysical microstructure', *Journal of Atmospheric and Oceanic Technology* **19**(5), 780–793.

Wyngaard, J., Rockwell, L. and Friehe, C. (1985), 'Errors in the measurement of turbulence upstream of an axisymmetric body', *Journal of Atmospheric and Oceanic Technology* **2**, 605 – 614.